The Astrophysical Journal, 754:5 (22pp), 2012 July 20 doi:10.1088/0004-637X/754/1/5

MID-INFRARED EXTINCTION MAPPING OF INFRARED DARK CLOUDS. II. THE STRUCTURE OF MASSIVE STARLESS CORES AND CLUMPS

Michael J. Butler[1] and Jonathan C. Tan[2]
[1] Department of Astronomy, University of Florida, Gainesville, FL 32611, USA
[2] Departments of Astronomy & Physics, University of Florida, Gainesville, FL 32611, USA
Received 2011 August 10; accepted 2012 May 11; published 2012 June 27

ABSTRACT

We develop the mid-infrared extinction (MIREX) mapping technique of Butler & Tan (Paper I), presenting a new method to correct for the Galactic foreground emission based on observed saturation in independent cores. Using *Spitzer* GLIMPSE 8 μm images, this allows us to accurately probe mass surface densities, Σ, up to $\simeq$0.5 g cm^{-2} with 2″ resolution and mitigate one of the main sources of uncertainty associated with Galactic MIREX mapping. We then characterize the structure of 42 massive starless and early-stage cores and their surrounding clumps, selected from 10 infrared dark clouds, measuring $\Sigma_{\rm cl}(r)$ from the core/clump centers. We first assess the properties of the core/clump at a scale where the total enclosed mass as projected on the sky is $M_{\rm cl} = 60\ M_\odot$. We find that these objects have a mean radius of $R_{\rm cl} \simeq 0.1$ pc, mean $\bar{\Sigma}_{\rm cl} = 0.3$ g cm^{-2} and, if fitted by a power-law (PL) density profile $\rho_{\rm cl} \propto r^{-k_{\rho,{\rm cl}}}$, a mean value of $k_{\rho,{\rm cl}} = 1.1$. If we assume a core is embedded in each clump and subtract the surrounding clump envelope to derive the core properties, then we find a mean core density PL index of $k_{\rho,c} = 1.6$. We repeat this analysis as a function of radius and derive the best-fitting PL plus uniform clump envelope model for each of the 42 core/clumps. The cores have typical masses of $M_c \sim 100\ M_\odot$ and $\bar{\Sigma}_c \sim 0.1$ g cm^{-2}, and are embedded in clumps with comparable mass surface densities. We also consider Bonnor–Ebert density models, but these do not fit the observed Σ profiles as well as PLs. We conclude that massive starless cores exist and are well described by singular polytropic spheres. Their relatively low values of Σ and the fact that they are IR dark may imply that their fragmentation is inhibited by magnetic fields rather than radiative heating. Comparing to massive star-forming cores and clumps, there is tentative evidence for an evolution toward higher densities and steeper density profiles as star formation proceeds.

Key words: dust, extinction – ISM: clouds – stars: formation

Online-only material: color figures

1. INTRODUCTION

Characterizing the initial conditions of massive star formation is important for distinguishing between various theoretical models. For example, McKee & Tan (2002, 2003, hereafter MT03) have presented the "Turbulent Core Accretion Model," which assumes that massive stars (including binaries and other low-order multiple systems) form from massive starless *cores* in a manner that can be considered a scaled-up version of the standard theory of low-mass star formation (Shu et al. 1987). The core undergoes global collapse to feed a central accretion disk. These massive starless cores are also assumed to be near virial equilibrium and in approximate pressure equilibrium with the surrounding *clump* environment, whose pressure is likely to be set by the self-gravitating weight of the gas, $P_{\rm cl} \simeq G\Sigma_{\rm cl}^2$, where $\Sigma_{\rm cl}$ is the mass surface density of the clump. The clump is defined to be the gas cloud that fragments to form a star cluster. Observed regions of massive star formation, including revealed massive star clusters where this activity occurred recently, have high values of $\Sigma_{\rm cl} \sim 1$ g cm^{-2} (but with a dispersion of about a factor of 10), implying large values of $P_{\rm cl}/k \gtrsim 10^8$ K cm^{-3}.

A massive, virialized core in pressure equilibrium with this environment cannot be supported by thermal pressure, given observed temperatures of $T \sim$ 10–20 K, and so must be supported by some form of nonthermal pressure, i.e., turbulence or magnetic fields. Since massive stars are "rare," in the sense that they constitute only a small mass fraction, ∼5%–10%, of the observed initial stellar mass function, then massive starless cores that will eventually form massive stars are also expected to be rare. Most massive structures are likely to fragment into clusters of lower-mass stars. We anticipate that preventing fragmentation of massive starless cores likely involves magnetic fields being strong enough such that the core mass is approximately equal to a magnetic critical mass and substructures are magnetically subcritical. Krumholz & McKee (2008) have argued that fragmentation is prevented by radiative heating from surrounding low-mass protostars, which requires them to have high accretion rates and thus for the clump to have a high value of $\Sigma \gtrsim 1$ g cm^{-2} in order to form massive stars. There is no such constraint if magnetic fields prevent fragmentation.

MT03 modeled massive cores as singular polytropic spheres, with a power-law (PL) density distribution of $\rho_c \propto r^{-k_{\rho,c}}$. There were few observational constraints on this density distribution, so MT03 assumed cores were part of a self-similar hierarchy of structure also shared by their surrounding clumps, where observations suggested $k_{\rho,{\rm cl}} \simeq 1.5$ (e.g., van der Tak et al. 2000; Beuther et al. 2002; Mueller et al. 2002). The parameters of a fiducial massive core make it clear why it is difficult to measure the structure observationally. For a 60 $M_\odot$ core embedded near the center of a clump with mean $\Sigma_{\rm cl} = 1$ g cm^{-2}, the radius is $R_c = 0.057\ M_{\rm c,60}^{1/2}(\Sigma_{\rm cl}/1\ {\rm g\ cm^{-2}})^{-1/2}$ pc. At typical distances, $\gtrsim$2 kpc, this radial size corresponds to $\lesssim$5.″9.

Until recently, measurements of mass surface densities of ∼1 g cm^{-2} (equivalent to $N_{\rm H} = 4.27 \times 10^{23}$ cm^{-2} or $A_V =$ 230 mag) were based mostly on millimeter dust continuum measurements, which require knowing the dust emissivity, dust temperature, and dust-to-gas ratio. In particular, the dust emissivity and temperature may be expected to vary along the

line of sight through a dense cloud. For total power observations with single dish telescopes, resolutions have been limited to $\sim 10''$, e.g., the diffraction limit of a 30 m telescope at 1.2 mm. Rathborne et al. (2006) carried out a study of this emission from 38 Galactic infrared dark clouds (IRDCs; these types of clouds are described in more detail below). The above considerations show that we do not expect their results to be able to resolve the scale of individual massive cores in high pressure environments, but are better suited to studying the properties of clumps that might form whole star clusters. Higher angular resolution has been achieved with interferometric observations, but these have been possible only toward relatively limited samples of objects, many of which are already in the process of forming a star (e.g., Bontemps et al. 2010).

The advent of space-based, MIR, high-photometric-accuracy, imaging surveys of the Galactic plane has opened up a new way to probe high mass surface density structures. Indeed, these cold, high Σ structures were first identified as "IRDCs" from analysis of *Infrared Space Observatory* (*ISO*; Perault et al. 1996) and the *Midcourse Space Experiment* (*MSX*; Egan et al. 1998) imaging data. With the *Spitzer Space Telescope*, more precise and higher angular resolution data became available. This led Butler & Tan (2009, hereafter BT09 or Paper I) to attempt to develop MIR extinction (MIREX) mapping as a precision technique for probing high mass surface density regions.

BT09 adopted the Ossenkopf & Henning (1994) thin ice mantle coagulated (for 10^5 yr at densities of 10^6 cm^{-3}, or equivalently for $\sim 10^6$ yr at densities of $\sim 10^5$ cm^{-3}) dust model for their fiducial analysis and a gas-to-(refractory component)-dust mass ratio of 156 (slightly higher than the value of 141 estimated by Draine (2011) from depletion studies). With these values, the opacity per unit gas mass in the IRAC band 4 at $\sim 8\ \mu$m of a source with a spectrum typical of Galactic diffuse MIR emission is $\kappa_{8\,\mu\mathrm{m}} = 7.48$ cm^2 g^{-1}. The fiducial value adopted by BT09 and in this paper is $\kappa_{8\,\mu\mathrm{m}} = 7.5$ cm^2 g^{-1}, so that

$$\tau_{8\,\mu\mathrm{m}} = \kappa_{8\,\mu\mathrm{m}}\Sigma = 7.5\left(\frac{\Sigma}{\mathrm{g\ cm^{-2}}}\right). \quad (1)$$

From the variety of dust models considered by BT09, we expect $\sim$30% uncertainties in the absolute value of $\kappa_{8\,\mu\mathrm{m}}$. Within a particular IRDC, we can expect some systematic variation in $\kappa_{8\,\mu\mathrm{m}}$ due to different degrees of ice mantle growth, but these should be at most $\sim$20% (Ossenkopf & Henning 1994), and probably much less after averaging over conditions on a line of sight through the cloud.

Apart from the choice of MIR opacity, there are two main sources of uncertainty involved in MIREX mapping. First, the intensity of the MIR emission behind the cloud is assumed to be smooth and must be estimated by extrapolation from nearby regions that are assumed to be extinction free. BT09 estimated that the extrapolation could lead to flux uncertainties of about 10%, corresponding to errors in $\Sigma \simeq 0.01\,\mathrm{g\,cm^{-2}}$, given fiducial dust models. This is a minimum Σ, below which MIREX mapping becomes unreliable. These problems of background estimation can be reduced by choosing IRDCs that are in regions of the Galactic plane where the observed surrounding emission is relatively constant and smooth around the cloud. One systematic bias that we expect to be present is caused by the fact that there will typically be some cloud material in the "envelope" region around the IRDC where extinction was assumed to be zero. From studies of CO emission around IRDCs (Hernandez & Tan 2011; Hernandez et al. 2011), we estimate that this envelope typically has $\Sigma \simeq 0.01$ g cm^{-2}. This is an additional reason why MIREX mapping becomes unreliable at low values of Σ. This problem can be addressed by combining MIR and NIR extinction mapping techniques (Kainulainen et al. 2011; Kainulainen & Tan 2012). The second major source of uncertainty is caused by foreground MIR emission along our line of sight to the IRDC. Neglecting this causes us to underestimate τ and thus Σ. The effect can be minimized by choosing IRDCs that are relatively nearby, as was done by BT09. BT09 also tried to estimate the expected amount of foreground emission, assuming it comes from a smoothly distributed population of small dust grains heated by massive stars that follow an exponential distribution in the Galaxy. For a cloud at a distance of 5 kpc at a Galactic longitude of $l \sim 30^\circ$, we estimate that 27% of the observed Galactic diffuse emission is from material in front of the cloud. For a part of the cloud that has Σ estimated to be ~ 0.1 g cm^{-2} in the absence of a foreground correction, applying this correction raises Σ by about a factor of two. If this foreground correction is not applied, then the largest values of Σ that can be derived are only ~ 0.2 g cm^{-2}. This model-dependent estimate of the foreground is quite uncertain and one of the main reasons that BT09 concentrated on nearby IRDCs. Poor understanding of the foreground emission is likely to limit the reliability of the mass surface densities and masses of IRDCs derived for large samples of objects (e.g., Simon et al. 2006; Peretto & Fuller 2009), especially for the more distant objects. Local heating of small dust grains that then produce MIR foreground emission cannot be accounted for in the BT09 model of foreground estimation and this can affect even nearby IRDCs. However, choosing relatively quiescent IRDCs can help minimize this particular source of uncertainty. One of the main goals of this paper is to introduce a new, improved method to measure the intensity of the foreground emission.

The structure of this paper is as follows. In Section 2, we introduce the method of saturation-based MIREX mapping. In Section 3, we present the results of applying this method to study the structure of 42 massive starless and early-stage core/clumps located in 10 IRDCs. In Section 4, we discuss the implications of these results for massive star and star cluster formation theories.

2. SATURATION-BASED MIR EXTINCTION MAPPING

The MIREX mapping technique requires knowing the intensity of radiation directed toward the observer at a location just behind the cloud of interest, $I_{\nu,0}$, and just in front of the cloud, $I_{\nu,1}$. Then, for negligible emission in the cloud and a simplified one-dimensional geometry,

$$I_{\nu,1} = e^{-\tau_\nu}\, I_{\nu,0}, \quad (2)$$

where the optical depth $\tau_\nu = \kappa_\nu \Sigma$, where κ_ν is the total opacity at frequency ν per unit gas mass and Σ is the gas mass surface density.

We cannot see $I_{\nu,0}$ directly, so it must be estimated by interpolation from surrounding regions. BT09 tried two main ways to do this using median filters. The large-scale median filter (LMF) method used a square filter of size $13'$ that was much larger than the IRDCs of interest so that the clouds did not significantly depress the estimated median intensity. This has the advantage of not assuming any prior knowledge about the IRDC, but the disadvantage of a coarse angular resolution of background intensity fluctuations. For studying specific IRDCs that can be defined as occupying a certain region of the sky, e.g., an ellipse, we thus introduced the small-scale median filter (SMF) method. Here, the size of the filter is set to be one-third

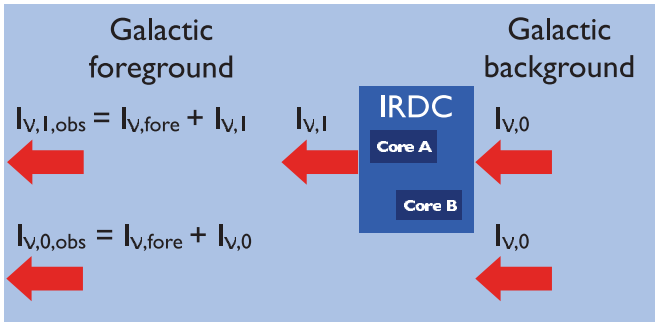

Figure 1. Schematic of simple one-dimensional model of radiative transfer through an IRDC, assuming negligible emission from the IRDC at frequency ν. If independent cores (i.e., localized density maxima) A and B are both of sufficiently high Σ, then $I_{\nu,1} \ll I_{\nu,\rm fore} \simeq I_{\nu,1,\rm obs}$(A, B), providing an accurate, empirical estimate of the foreground intensity to the IRDC.

(A color version of this figure is available in the online journal.)

of the major axis of the IRDC ellipse (defined by Simon et al. 2006), but it is only applied for background estimation outside of the IRDC ellipse. Inside the ellipse, we estimate the background by interpolating from the surrounding background model. BT09 estimated that the uncertainties in background estimation due to this interpolation were at a level of $\lesssim$10%, which corresponds to $\Sigma \lesssim 0.013$ g cm^{-2}.

However, because of foreground emission toward the IRDC, we actually observe (see Figure 1)

$$I_{\nu,1,\rm obs} = I_{\nu,\rm fore} + I_{\nu,1} = I_{\nu,\rm fore} + e^{-\tau_\nu}\, I_{\nu,0}, \quad (3)$$

and toward the IRDC surroundings, where we are trying to estimate $I_{\nu,0}$, we actually observe

$$I_{\nu,0,\rm obs} = I_{\nu,\rm fore} + I_{\nu,0}. \quad (4)$$

The primary uncertainty in the MIREX mapping method of BT09 for larger values of Σ is the estimate of the level of the foreground contribution to the intensity, $I_{\nu,\rm fore}$. In order to increase the method's sensitivity to higher values of mass surface density, we now describe a new, empirical method to estimate this contribution.

If a core has a high enough mass surface density, then it will block essentially all the background emission. The observed minimum intensity in the cloud will then be approximately equal to the foreground emission and the angular distribution of this intensity may appear to flatten or "saturate." It is difficult to be certain if an individual dense core is saturated (as is sometimes assumed if the foreground is simply estimated from the darkest pixel; e.g., Ragan et al. 2009). However, we propose that if the minimum intensity is observed to "be the same" in two or more "independent" cores (i.e., spatially resolved peaks in Σ) in the same cloud, then this is very likely due to saturation. In practice, by "be the same," we adopt the condition to be within 2σ of each other, where σ is the uncertainty in the GLIMPSE 8 μm intensities of 0.6 MJy sr^{-1} (Reach et al. 2006). By "independent," we adopt an angular separation of at least 8″, i.e., much larger than the 2″ FWHM of the *Spitzer* IRAC 8 μm point-spread function (PSF).

The algorithm for this method is as follows (see also Figure 1).

1. Define a region of the sky as the "IRDC." Following BT09, we use the ellipses from the catalog of Simon et al. (2006), which were based on *MSX* images.
2. Using GLIMPSE 8 μm images, find the minimum value of $I_{\nu,1,\rm obs}$ inside the IRDC, $I_{\nu,1,\rm obs}$(min).
3. Search for all pixels in the IRDC with $I_{\nu,1,\rm obs}$(min) $< I_{\nu,1,\rm obs} < I_{\nu,1,\rm obs}$(min) $+ 2\sigma$. If there are pixels meeting these criteria that are independent (to be conservative we adopt $\geqslant$8″ away from the IRDC minimum), then the IRDC is defined to be saturated, all the above pixels are labeled as "saturated pixels," and the following steps are carried out.
4. The mean value of $I_{\nu,1,\rm obs}$ of the saturated pixels is evaluated, $I_{\nu,1,\rm obs}$(sat). We set the foreground intensity (which includes all sources of emission: Galactic, zodiacal, and instrumental; Battersby et al. 2010) to be $I_{\nu,\rm fore} = I_{\nu,1,\rm obs}$(sat) $- 2\sigma$. This subtraction is motivated to have $I_{\nu,\rm fore} < I_{\nu,1,\rm obs}$(min) and thus give every pixel a finite value of τ, and thus Σ.

If all the "saturated pixels," defined above, really did have negligible values of $I_{\nu,1}$ and had a distribution of intensities that was relatively uniform in the above range, then $I_{\nu,\rm fore} \simeq I_{\nu,0,\rm obs}$(min) $+ 1\sigma$ and our method would be underestimating $I_{\nu,\rm fore}$ by $2\sigma = 1.2$ MJy sr^{-1}. In fact, we do find for the $\sim$300 "saturated pixels" in the 10 IRDCs of our sample, a mean value of $I_{\nu,1,\rm obs} - I_{\nu,1,\rm obs}$(min) $\simeq 0.7$ MJy sr^{-1}. Thus, we are likely to be underestimating $I_{\nu,\rm fore}$ (overestimating $I_{\nu,1}$) by an amount of $\simeq 2\sigma = 1.2$ MJy sr^{-1}. This leads to a value of Σ where our measured values are significantly affected by saturation:

$$\Sigma(\rm sat) = \frac{\tau_\nu(\rm sat)}{\kappa_\nu} = \frac{\ln(I_{\nu,0}/I_{\nu,1})}{\kappa_\nu}, \quad (5)$$

where $I_{\nu,1}/I_{\nu,0} = I_{8\,\mu\rm m,1}/I_{8\,\mu\rm m,0} = e^{-\tau_{8\,\mu\rm m}(\rm sat)}$ so $\tau_{8\,\mu\rm m}$(sat) $= \ln(I_{\nu,0}/I_{\nu,1})$, that is set by $I_{\nu,1} = 2\sigma \rightarrow 1.2$ MJy sr^{-1}. For a typical IRDC with $I_{\nu,0,\rm obs} = 100$ MJy sr^{-1}, $I_{\nu,\rm fore} = f_{\rm fore} I_{\nu,0,\rm obs} = 30$ MJy sr^{-1} so that $I_{\nu,0} = 70$ MJy sr^{-1}, then $\tau_{8\,\mu\rm m}$(sat) $= 4.07$ and Σ(sat) $= 0.544$ g cm^{-2}. For a region of such a cloud with a true value of $\Sigma = 0.5$ g cm^{-2} so that $I_{\nu,1} = 1.65$ MJy sr^{-1}, if we have underestimated $I_{\nu,\rm fore}$ by 1.2 MJy sr^{-1}, then we would infer $\Sigma = 0.427$ g cm^{-2}. Similarly, for a true $\Sigma = 0.4$ g cm^{-2}, we would infer $\Sigma = 0.361$ g cm^{-2}. The values of Σ(sat) calculated with $I_{8\,\mu\rm m,1} = 1.2$ MJy sr^{-1} for the 10 IRDCs in our sample are listed in Table 1. They range from Σ(sat) $= 0.33$ to 0.52 g cm^{-2} as one progresses along the Galactic plane toward $l = 0$, where the background is brightest.

An additional uncertainty results from our use of a single effective value of $\kappa_{8\,\mu\rm m} = 7.5$ cm^2 g^{-1} averaged over the *Spitzer* IRAC 8 μm band, weighting by the filter response function, the spectrum of the Galactic background and the dust opacity model (BT09). Since these functions vary over this wavelength range (see Figure 1 of BT09), at large optical depths the actual transmitted intensity will be greater than that predicted, being more dominated by the region of the spectrum with the lowest opacity. The net effect is an underestimation of the true mass surface density, given the observed ratio of transmitted to incident intensities. We have investigated the size of this effect by integrating the transfer Equation (2) over the above weighting functions (see Figure 2). For our fiducial dust model (the moderately coagulated thin ice mantle model of OH94), which has a relatively flat MIR opacity law, the effect is small: just a few percent effect up to a value of $\Sigma \sim 1$ g cm^{-2}, rising to about a 10% effect by $\Sigma = 10$ g cm^{-2}. For illustrative purposes, Figure 2 also shows the results for the Draine (2003) $R_V = 3.1$ dust model, more appropriate for the diffuse ISM, which has bare grains and stronger variation of opacity across this wavelength range. Now the effect leads to an underestimation of Σ by up to several tens of percent for $\Sigma \sim 1$ g cm^{-2}. Other dust models we have considered, such as the Draine (2003) $R_V = 5.5$ model, have somewhat smaller underestimation factors.

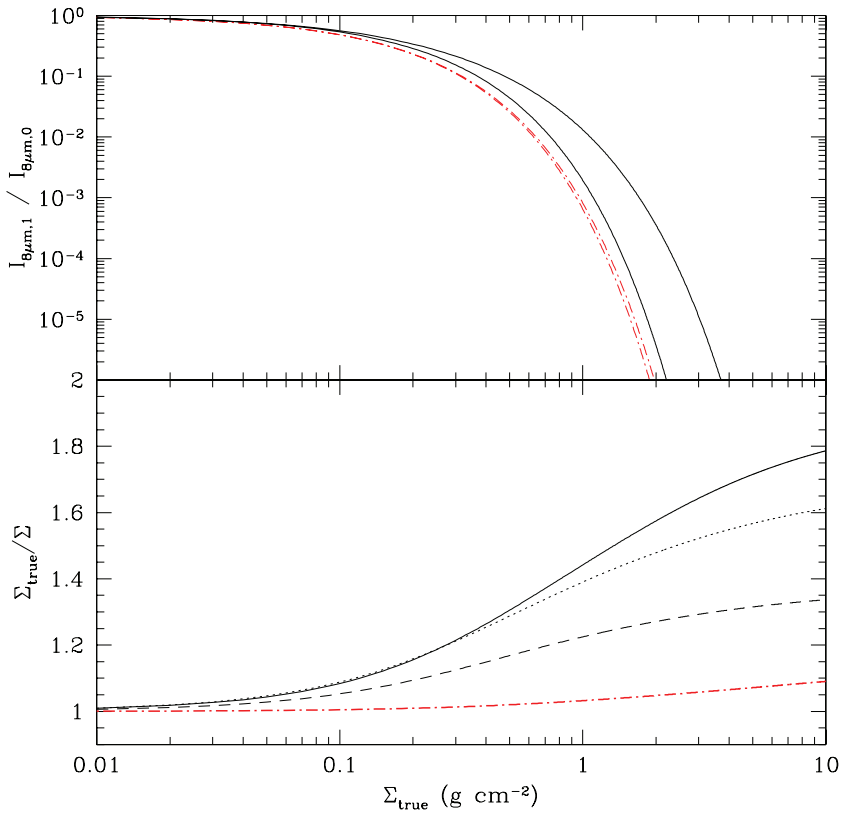

Figure 2. Effect of finite filter width on estimates of Σ and accuracy of an approximation using a single band-averaged opacity (see the text). The *Spitzer* IRAC band 4, i.e., 8 μm, filter has sensitivity from about 6.5–9.5 μm. Top panel: ratio of transmitted to incident flux as a function of true mass surface density, $\Sigma_{\rm true}$. The result for the band-averaged opacity for the moderately coagulated thin ice mantle dust model of OH94 (our fiducial model) is shown by the lower red dot-dashed line. The actual transmitted flux, calculated by integrating the transfer equation over the bandpass, is shown by the upper red dot-dashed line. The equivalent quantities for the Draine (2003) $R_V = 3.1$ dust model are shown by the lower and upper black solid lines: the effect is larger here as this dust model shows larger opacity variations across the band. Bottom panel: effect on estimation of Σ. Given an observed ratio of transmitted to incident intensities, the true mass surface density, $\Sigma_{\rm true}$, will be greater than that estimated using the band-averaged opacity, Σ. The ratio of $\Sigma_{\rm true}/\Sigma$ is shown by the red dot-dashed line for the above OH94 thin ice mantle model. The OH94 uncoagulated thin ice mantle model gives essentially the same result. The error is a few percent in the region of interest of the IRDC cores in this study. Also shown are these effects for the Draine (2003) $R_V = 3.1$ (black solid line), $R_V = 5.5$ (black dotted line), and $R_V = 5.5$ case B (black dashed line).

(A color version of this figure is available in the online journal.)

Table 1
Infrared Dark Cloud Sample[a]

Cloud Name	l (°)	b (°)	d (kpc)	$R_{\rm eff}$ (pc)	e	P.A. (°)	$\bar{I}_{\nu,0,\rm obs}$[b] (MJy sr^{-1})	$f_{\nu,\rm fore}$	$f_{\nu,\rm fore}^{\rm BT09}$	Σ(sat) (g cm^{-2})	$\bar{\Sigma}_{\rm SMF}$[c] (g cm^{-2})	$\bar{\Sigma}_{\rm SMF}^{\rm BT09}$ (g cm^{-2})	$M_{\rm SMF}$ ($M_\odot$)	$M_{\rm SMF}^{\rm BT09}$ ($M_\odot$)
A (G018.82−00.28)	18.822	−0.285	4.8	10.4	0.961	74	93.8	0.472	0.209	0.496	0.0489	0.0355	17,700	7,600
B (G019.27+00.07)	19.271	0.074	2.4	2.71	0.977	88	85.1	0.452	0.075	0.488	0.0814	0.0387	2,200	830
C (G028.37+00.07)	28.373	0.076	5.0	15.4	0.632	78	89.9	0.339	0.266	0.520	0.0610	0.0527	45,000	42,000
D (G028.53−00.25)	28.531	−0.251	5.7	16.9	0.968	60	71.5	0.559	0.327	0.436	0.0525	0.0418	53,400	27,000
E (G028.67+00.13)	28.677	0.132	5.1	11.5	0.960	103	96.7	0.455	0.276	0.504	0.0593	0.0543	25,200	19,400
F (G034.43+00.24)	34.437	0.245	3.7[d]	3.50	0.926	79	48.4	0.601	0.193	0.370	0.0994	0.0371	4,460	1,670
G (G034.77−00.55)	34.771	−0.557	2.9	3.06	0.953	95	43.2	0.624	0.140	0.347	0.0648	0.0420	2,010	1,140
H (G035.39−00.33)	35.395	−0.336	2.9	9.69	0.951	59	45.6	0.405	0.142	0.416	0.0479	0.0262	13,340	6,800
I (G038.95−00.47)	38.952	−0.475	2.7	3.73	0.917	64	42.1	0.418	0.141	0.402	0.0707	0.0616	2050	1,490
J (G053.11+00.05)	53.116	0.054	1.8	0.755	0.583	50	28.6	0.509	0.121	0.328	0.125	0.0699	259	80

Notes.

[a] Coordinate names, Galactic coordinates, kinematic distances, effective radii (of equal area circles), eccentricities, and position angles of fitted ellipses are from Simon et al. (2006). We then compare quantities derived in this paper with those from BT09.

[b] Mean intensity of the SMF background model (BT09) inside the Simon et al. (2006) ellipse.

[c] Areal average of those pixels for which values of $\Sigma_{\rm SMF} > 0$ are derived. Estimates of a mean mass surface density based on $M_{\rm SMF}$ and $R_{\rm eff}$ are typically much smaller because of the regions inside the clouds ellipse with derived $\Sigma_{\rm SMF} \leqslant 0$ (see BT09).

[d] The distance to IRDC F has recently been estimated from parallax of radio sources to be 1.56 ± 0.12 kpc (Kurayama et al. 2011), a factor of 0.42 smaller than the kinematic distance of Simon et al. (2006). For consistency with BT09, we retain the kinematic distance, but the mass of this cloud and its cores are likely to need to be reduced by a factor of 0.178.

A further additional systematic uncertainty results from the fact that the foreground intensity will vary across the IRDC, especially due to local radiation sources. The accuracy of the Σ values will be higher in regions closer to the locations of saturated cores where $I_{\nu,\rm fore}$ has been estimated and in IRDCs with minimal local heating sources.

3. RESULTS

3.1. IRDC Properties

Following the above algorithm, we find that all 10 IRDCs of the BT09 sample exhibit the effects of saturation. In hindsight, this is not too surprising since these clouds were selected to have relatively high contrast against the background. The Σ maps of the clouds are shown in Figures 3 and 4. The properties of these clouds are listed in Table 1, where we also compare their properties to those derived with the SMF method of BT09 with the analytic model of foreground estimation. Using the saturation-based estimate of foreground emission, we find that $I_{\nu,\rm fore}$ and thus $f_{\rm fore}$ has increased in all the clouds. Thus, the highest values of Σ that we infer have risen from ∼0.1–0.3 g cm^{-2} in BT09 to ∼0.4–0.6 g cm^{-2} in this paper. The mean values, $\bar{\Sigma}_{\rm SMF}$, rise by smaller factors, so that the total cloud masses rise by on average a factor of 2.0. A comparison of the global properties of these IRDC with the predictions of theoretical models of the interstellar medium will be presented in a separate paper.

3.2. Massive Starless Cores and Clumps

3.2.1. Locating the Cores

The cores we are considering are a subset of those originally identified by Rathborne et al. (2006) based on their millimeter dust continuum emission, observed with the IRAM 30 m Telescope at 11″ FWHM angular resolution. BT09 selected 43 cores from the Rathborne et al. sample, excluding those with significant 8 μm emission and those with low-contrast against the MIR background (i.e., with $\Sigma \lesssim 0.02$ g cm^{-2}). Here, we have excluded one of the BT09 cores, E4, because its GLIMPSE image suffers from a diagonal boundary artifact where the intensity of the diffuse emission changes abruptly.

BT09 treated the cores as circular with radii equal to half the reported FWHM diameter of Gaussian fits that Rathborne et al. (2006) fitted to their millimeter continuum images. These circles were centered at the coordinates estimated by Rathborne et al. As discussed in Section 3.1, we expect our derived values of Σ to be higher (and more accurate) than those of BT09. Comparing the core masses of BT09 with those derived here for the same regions, we find they have typically increased by a factor of about 2.2.

In this paper, we now redefine the core center to be the center of the highest Σ pixel inside the previous core boundary. If there are two or more adjacent saturated pixels at the core center, then their average position is used to define the center. In fact, 17 of the 42 cores exhibit saturation. Occasionally, after inspecting the 8 μm GLIMPSE and 24 μm MIPSGAL images, we note the presence of MIR sources near (<7.″5) the core center. This occurs in 9 of the 42 cores (B2, C6, C8, D5, D6, D8, E2, E3, and I1). In order to focus on massive starless and early-stage cores, we shift the center to a new, nearby ($\lesssim$3″) Σ maximum to avoid any major sources of MIR emission within a radius of 7.″5 of the new center. In several cases (C4, D4, F2, and J1), the Σ map inside the Rathborne et al. (2006) core boundary does not exhibit a well-defined high Σ peak. In these cases, we select a new core center as close as possible to the Rathborne et al. core: normally, this is within a few arcseconds of the boundary, but for F2 it is about 10″ outside.

Figure 5(a) shows the Σ map of Core A1, extracted from the larger image of IRDC A, shown in Figure 3(a). Pixels suffering from saturation are marked with small white squares. The core center is marked with a cross. Similar images of all 42 cores are shown in Figures 6–12.

We note that five of the IRDCs (B, E, G, H, and J) only have one core that exhibits saturation. This is possible because the condition to determine if an IRDC is saturated is based on independent positions (separated by at least 8″) having the same foreground intensity (to within 2σ), rather than requiring two cores to meet this condition. The 42 cores we have selected for analysis are not meant to be a complete census of all the dense regions in these IRDCs. For example, IRDC J only has one core selected.

The core Σ maps exhibit complex structure. It is not easy to define the boundary of a core from its surrounding clump, especially when one recalls that we are viewing a three-dimensional structure in projection. ^{13}CO(1–0) data exist for these IRDCs via the Galactic Ring Survey (Jackson et al. 2006), but with poor angular resolution (∼46″). Also, in the cores, we expect CO to be highly depleted from the gas phase due to freezeout onto dust grain surfaces. Widespread CO depletion has been observed in IRDC H by comparing our Σ map with C^{18}O emission observed with the IRAM-30m Telescope (Hernandez et al. 2011). Fontani et al. (2011) observed N_2H^+, which does not freeze out so readily as CO, from four of our cores (C1, F1, F2, and G2), but again with relatively poor angular resolution (>10″). Thus, given the lack of high angular resolution molecular line data for all the cores, here we present a uniform analysis of core structure based only on the extinction maps.

For simplicity, we first make radial profiles of mean total mass surface density, which we refer to as $\Sigma_{\rm cl}$ since it includes contribution from the clump (see below), considering a series of annuli extending from the core center with width equal to 1 pixel, i.e., 1.″2. Fractional overlap of pixels with these annuli is accounted for. "Holes" in the Σ maps due to MIR sources are treated as having a zero, i.e., negligible, value. In general, these sources do not significantly affect our characterization of core structure, at least in the inner ∼7.″5, since we have chosen cores that are relatively free of strong sources (E3 is the worst affected, and is somewhat exceptional in this regard). Larger annuli are minimally affected by individual MIR sources, which cover only a small fraction of the area. We extend the radial profiles out to a maximum angular scale equal to that reported by Rathborne et al. (2006) based on millimeter dust emission, i.e., a radius equal to one FWHM of their fitted Gaussian profile. As we will see, this is generally larger than the scale over which the core can be considered to be a single monolithic object.

For Core A1, Figure 5(b) shows $\Sigma_{\rm cl}(r)$ with blue open square symbols, plotted at the radii corresponding to the center of each annulus. The total enclosed mass, which we refer to as the clump mass $M_{\rm cl}(r)$, is indicated by the blue long-dashed line.

3.2.2. Core and Clump Properties at the 60 $M_\odot$ Enclosed Mass Scale

Before considering a more detailed analysis of the radial structure, it is instructive to first consider the properties of these core/clump objects at a scale where the total mass enclosed is $M_{\rm cl} = 60\ M_\odot$. If all this mass were in a core, then such a core has the potential to form a ∼30 $M_\odot$ star, given expected star formation efficiencies of ∼50% due to protostellar outflows

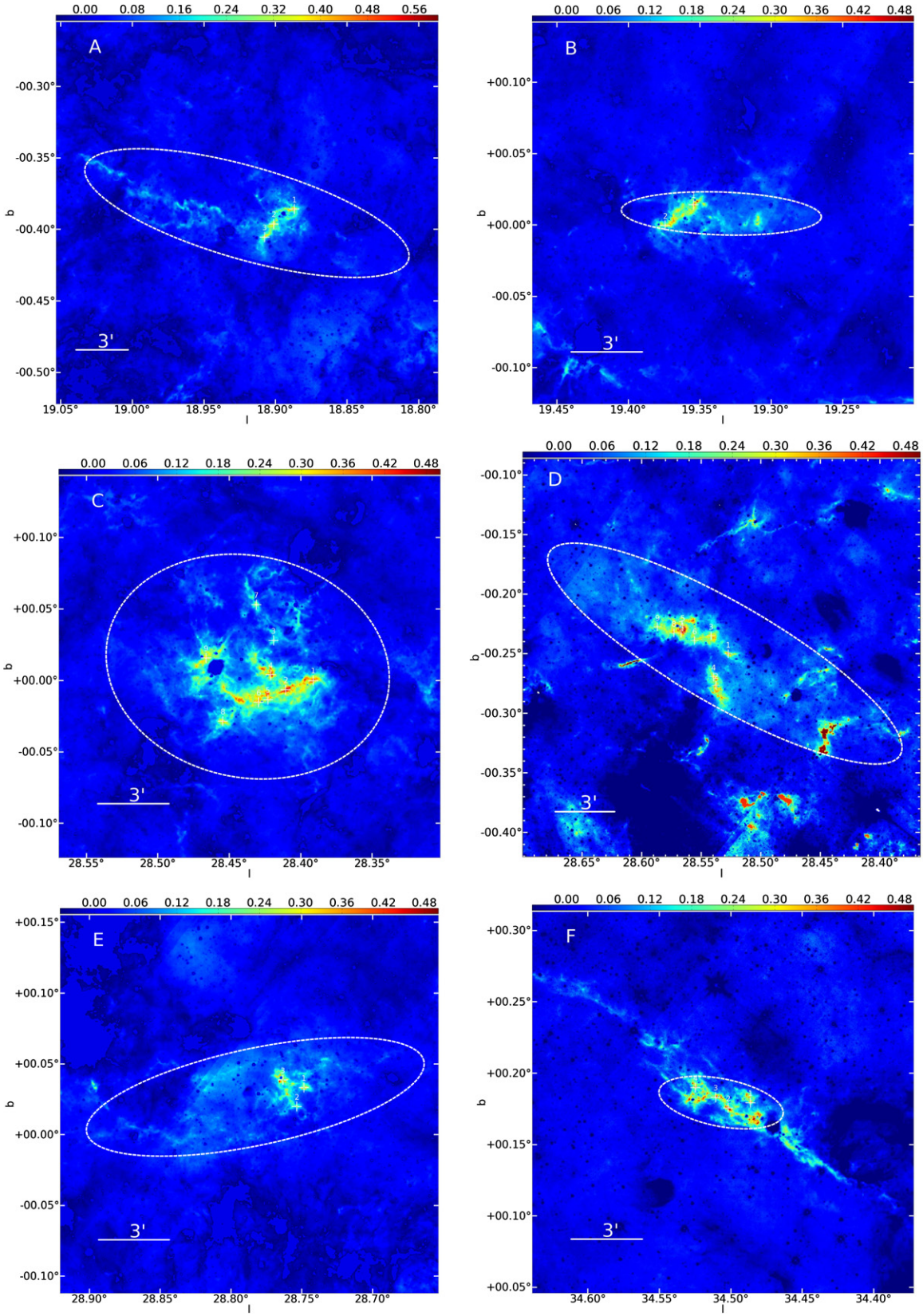

Figure 3. Mass surface density, $\Sigma_{\rm SMF}$, maps of IRDCs A–F derived from MIREX mapping using *Spitzer* IRAC 8 μm images with pixel scale of 1.″2 and angular resolution of 2″ using a saturation-based estimate of the foreground emission (Section 2). The color scale is indicated in g cm^{-2}. The dashed ellipse, defined by Simon et al. (2006) based on *MSX* images, defines the region where the background emission is estimated not directly from the small-scale median filter average of the image intensity, but rather by interpolation from nearby regions just outside the ellipse. The locations of the massive starless cores we have selected for analysis (Section 3) are marked with crosses. Bright MIR sources appear as artificial "holes" in the map, where we have set the values of $\Sigma = 0$ g cm^{-2}.

(A color version of this figure is available in the online journal.)

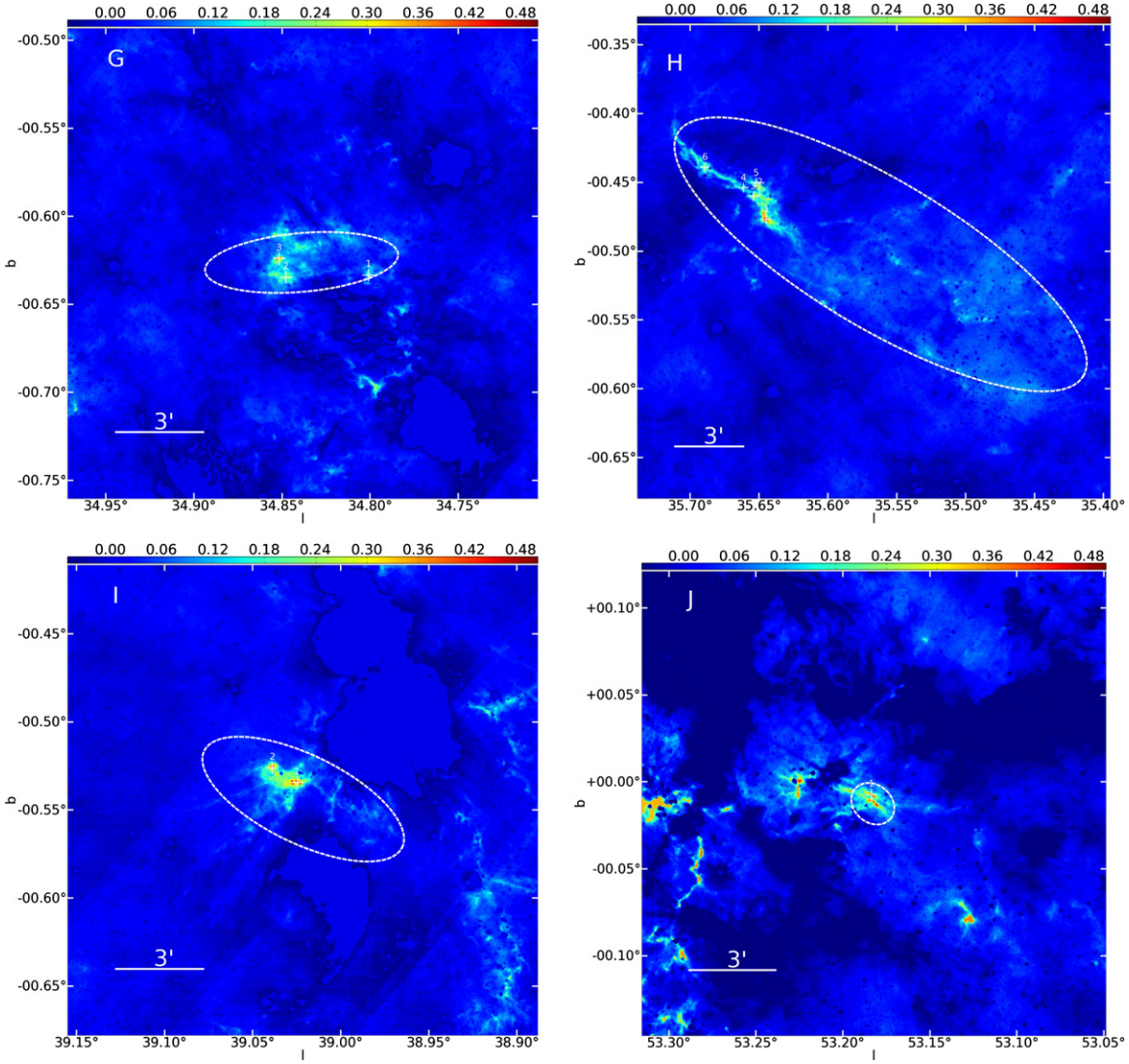

Figure 4. Mass surface density, $\Sigma_{\rm SMF}$, maps (in the same format as Figure 3) of IRDCs G–J derived from MIREX mapping using *Spitzer* IRAC 8 μm images. (A color version of this figure is available in the online journal.)

(J. C. Tan & C.F. McKee, in preparation). Note that there is of course no guarantee that all our sources will collapse in this way and on statistical grounds one would not expect them to: most are likely to undergo fragmentation to form lower-mass stars.[3] For Core A1, 60 $M_\odot$ is enclosed within $R_{\rm cl} = 0.0962$ pc, so at this scale $\bar{\Sigma}_{\rm cl} = 0.431$ g cm^{-2}. A black dashed circle with this radius is shown in Figure 5(a) and these core properties are listed in Table 2. Core A1 happens to be one of the most extensively saturated cores at the scale of an enclosed mass of 60 $M_\odot$ (along with C2, H1, I1, I2, and J1), so these numbers are likely to be significantly affected by saturation (which causes us to underestimate Σ), so actually the radius enclosing 60 $M_\odot$ would be smaller and $\bar{\Sigma}$ larger.

The distributions of the radii, $R_{\rm cl}$, and mean mass surface densities, $\bar{\Sigma}_{\rm cl}$, of the 42 core/clumps at the $M_{\rm cl} = 60\ M_\odot$ scale are shown in Figure 13(a) (with the six highly saturated cores—A1, C2, H1, I1, I2, and J1—shown as a shaded subset). The mean/median/rms dispersion-about-the-mean of $R_{\rm cl}(M_{\rm cl} = 60\ M_\odot) = 0.121/0.114/0.0238$ pc. The mean/median/rms dispersion values of $\bar{\Sigma}_{\rm cl}(M_{\rm cl} = 60\ M_\odot) = 0.296/0.318/0.0952$ g cm^{-2} (see also Table 3).

We next fit a PL density distribution,

$$\rho_{\rm cl}(r) = \rho_{\rm s,cl}\left(\frac{r}{R_{\rm cl}}\right)^{-k_{\rho,\rm cl}}, \quad (6)$$

where $\rho_{\rm s,cl} = \mu_{\rm H} n_{{\rm H},s,{\rm cl}}$ (with $\mu_{\rm H} = 2.34\times10^{-24}$ g) is the density at the surface of the clump, $R_{\rm cl}$. We project the above distribution to derive $\Sigma_{\rm cl}(r)$, which we then convolve with a Gaussian with an FWHM of 2″ (to allow for the *Spitzer* IRAC 8 μm PSF). We then fit this model to the observed $\Sigma_{\rm cl}(r)$ profile, excluding annuli that are significantly (>50%) affected by saturated pixels. For Core A1, $k_{\rho,\rm cl} = 1.40$ and $n_{{\rm H},s,{\rm cl}} = 2.47\times10^5$ cm^{-3}. For the whole sample, the mean/median/dispersion values of $k_{\rho,\rm cl} = 1.09/1.10/0.236$ and $n_{{\rm H},s,{\rm cl}} = (1.76/1.85/0.852)\times10^5$ cm^{-3}. These distributions are shown in Figure 13(a) with the blue dotted histograms. The values for individual cores are listed in Table 2.

The above analysis is somewhat simplistic in that it has assumed the structure exists in isolation. In reality, we see that

[3] One cannot distinguish between massive star formation Core Accretion and Competitive Accretion theories (Bonnell et al. 2001) simply by observing that a massive structure is actually composed of sub-fragments (see Bontemps et al. 2010, their Section 4.6).

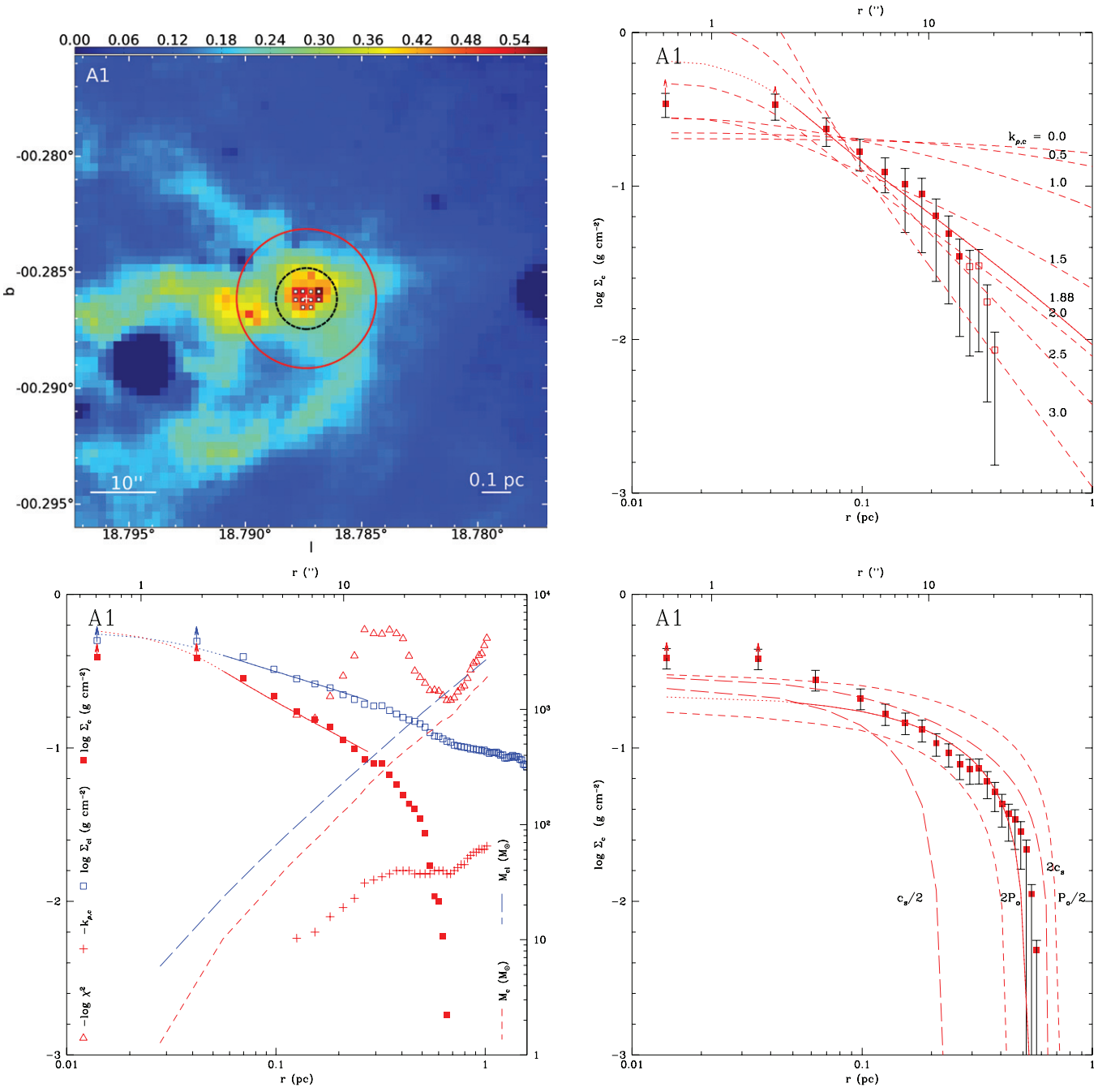

Figure 5. (a) Top left: mass surface density, $\Sigma_{\rm SMF}$, map in g cm^{-2} of IRDC Core A1, extracted from the map of IRDC A (Figure 3). The core center is marked with a cross. Saturated pixels, for which Σ is a lower limit of the true value, are marked with small white squares. The black dashed circle shows the radius enclosing a total mass of 60 $M_\odot$. The red solid circle shows the extent of the core derived from the best-fit power-law (PL) core plus envelope model (see the text). (b) Bottom left: radial profiles of Core A1: observed log $\Sigma_{\rm cl}/({\rm g\ cm^{-2}})$ (blue open squares, plotted at annuli centers) derived from the map shown in (a); total projected enclosed mass, $M_{\rm cl}$, (blue long-dashed line (see right axis)); core mass, M_c after clump envelope subtraction (red dashed line (see right axis)); index of core PL density profile, $k_{\rho,c}$, (red crosses); $-\log\,\chi^2$ (red triangles) of the PL plus envelope fit (best fit has a maximum or local maximum value (see the text)); the best-fit PL plus envelope model (blue solid line; dotted line shows range affected by saturation that was not used in the fitting); log $\Sigma_c/({\rm g\,cm^{-2}})$ of best-fit core after envelope subtraction (red solid squares) and PL fit (red solid line; dotted line shows range affected by saturation that was not used in the fitting). (c) Top right: $\Sigma_c(r)$, i.e., after clump envelope subtraction for the best-fit model (red solid squares; open squares show residual, post-subtraction envelope material). PL models with various values of $k_{\rho,c}$ are indicated (dashed lines), including the best-fit model with $k_\rho = 1.88$ (solid line). (d) Bottom right: as for (c), but for Bonnor–Ebert (BE) plus envelope fitting. $\Sigma_c(r)$, i.e., after clump envelope subtraction for the best-fit model (red solid squares). Best-fit BE model (solid line) and models varying c_s (long-dashed lines) and P_0 (dashed lines) by factors of two from this are shown (see the text).

(A color version of this figure is available in the online journal.)

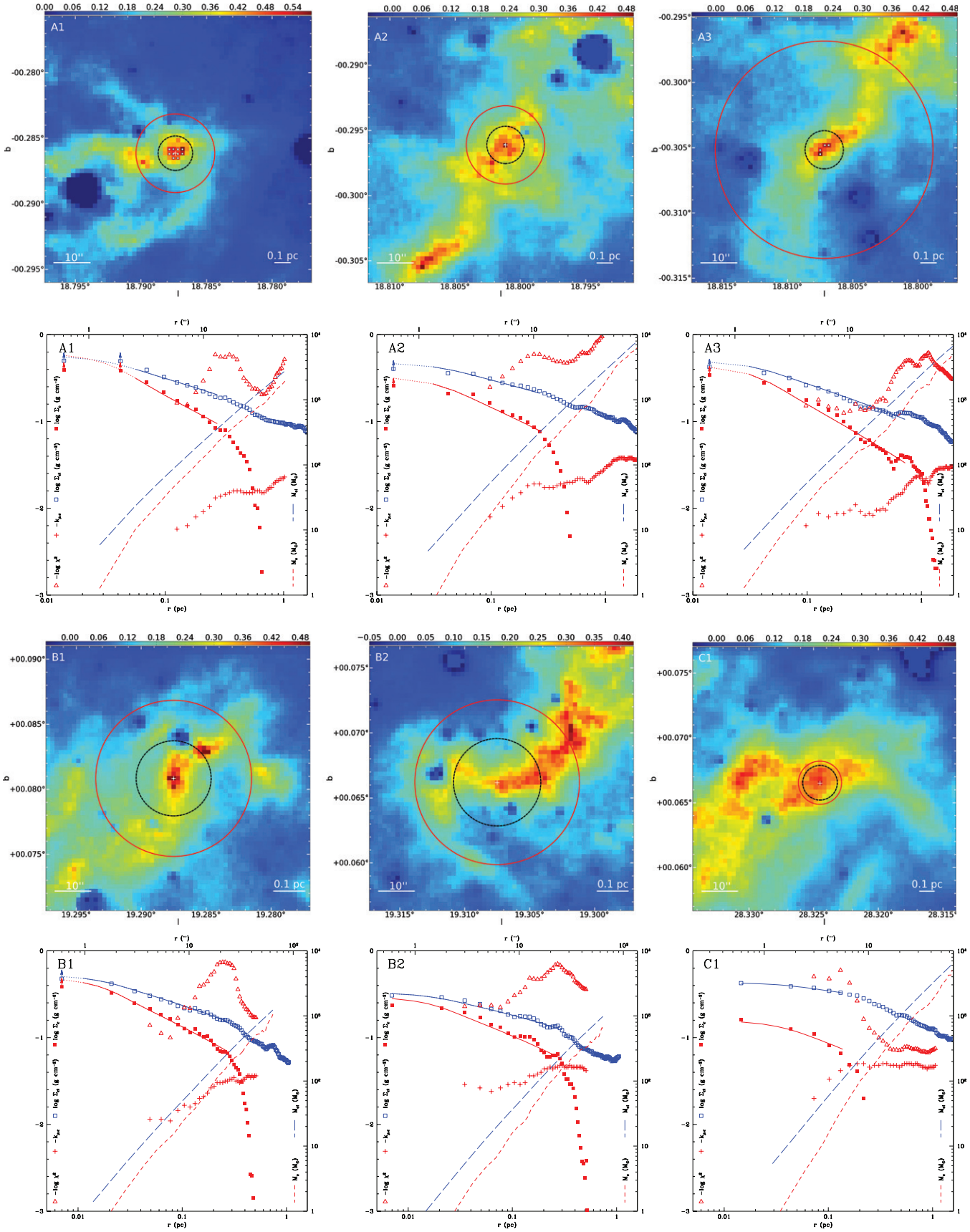

Figure 6. Core A1, A2, A3, B1, B2, and C1 Σ maps (notation as in Figure 5(a)) and azimuthally averaged radial profile figures (notation as in Figure 5(b)). (A color version of this figure is available in the online journal.)

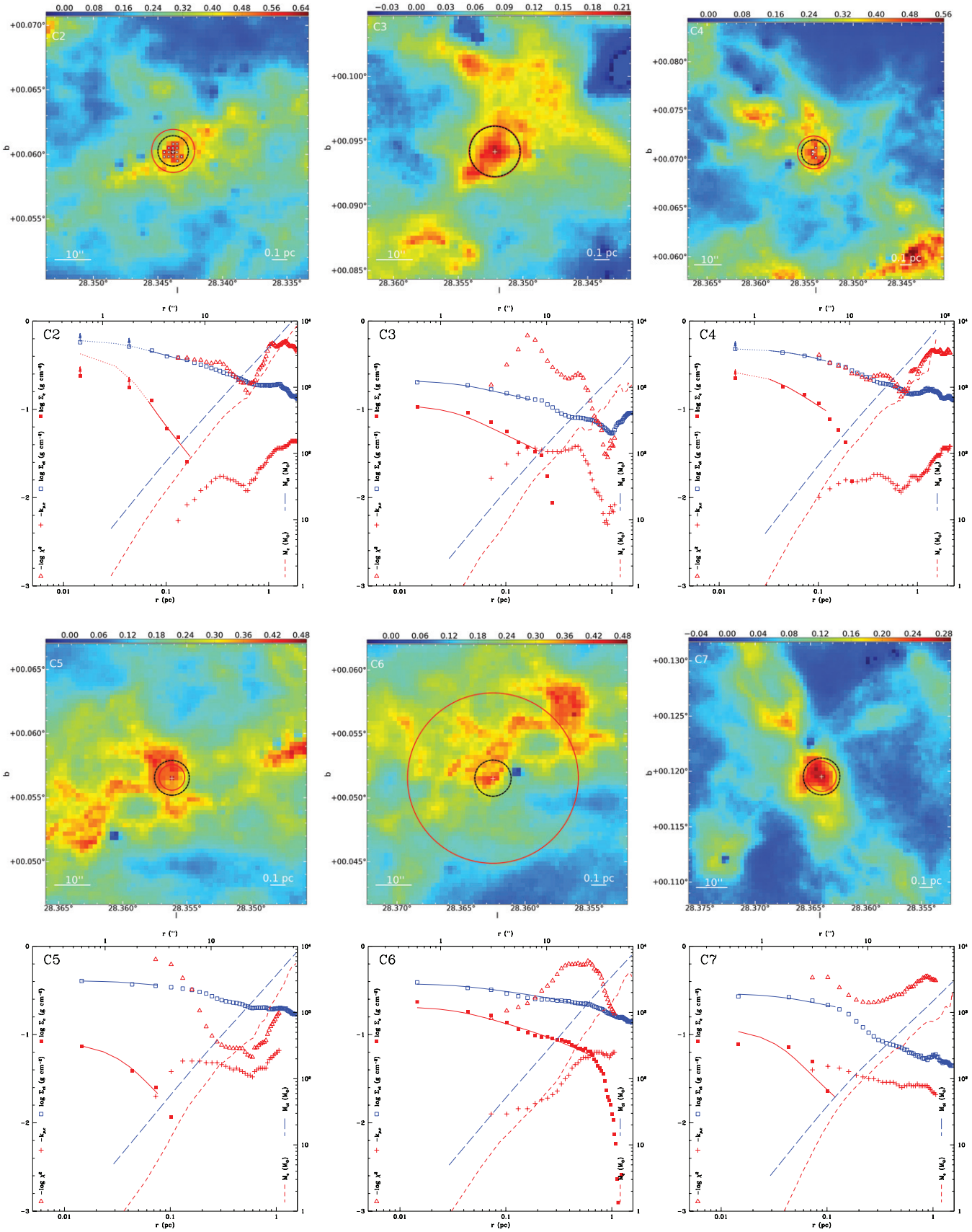

Figure 7. Core C2, C3, C4, C5, C6, and C7 Σ maps (notation as in Figure 5(a)) and azimuthally averaged radial profile figures (notation as in Figure 5(b)). (A color version of this figure is available in the online journal.)

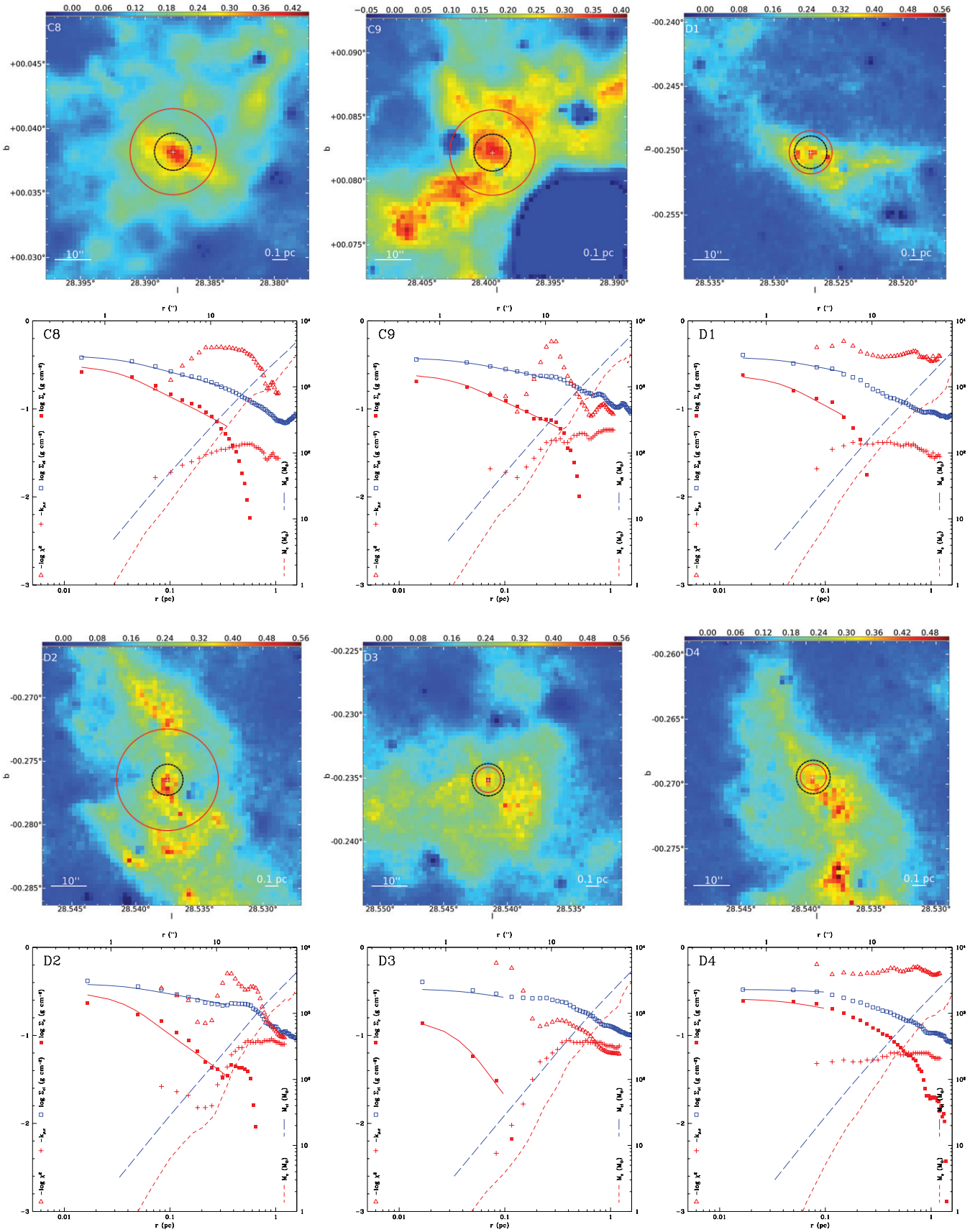

Figure 8. Core C8, C9, D1, D2, D3, and D4 Σ maps (notation as in Figure 5(a)) and azimuthally averaged radial profile figures (notation as in Figure 5(b)). (A color version of this figure is available in the online journal.)

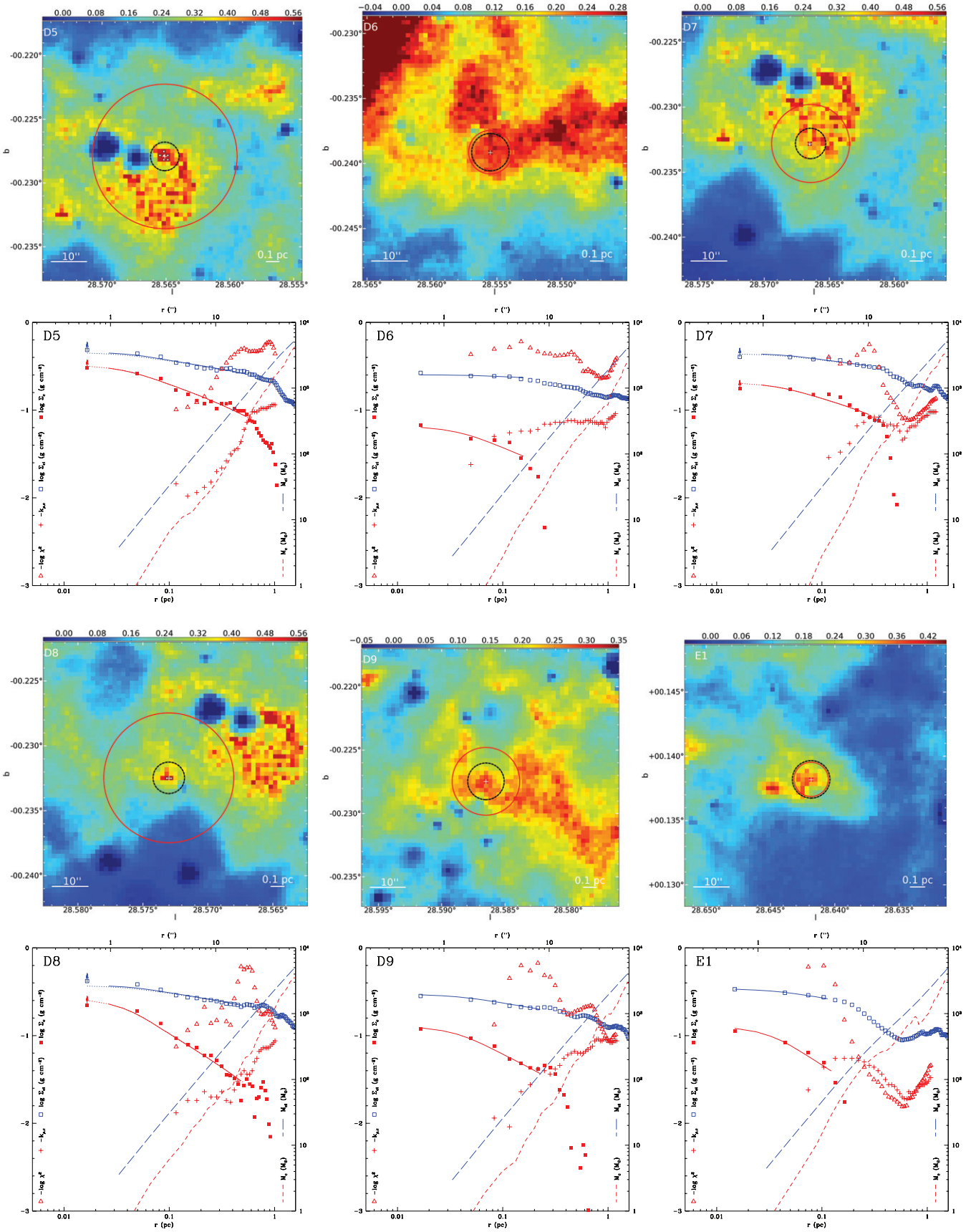

Figure 9. Core D5, D6, D7, D8, D9, and E1 Σ maps (notation as in Figure 5(a)) and azimuthally averaged radial profile figures (notation as in Figure 5(b)). (A color version of this figure is available in the online journal.)

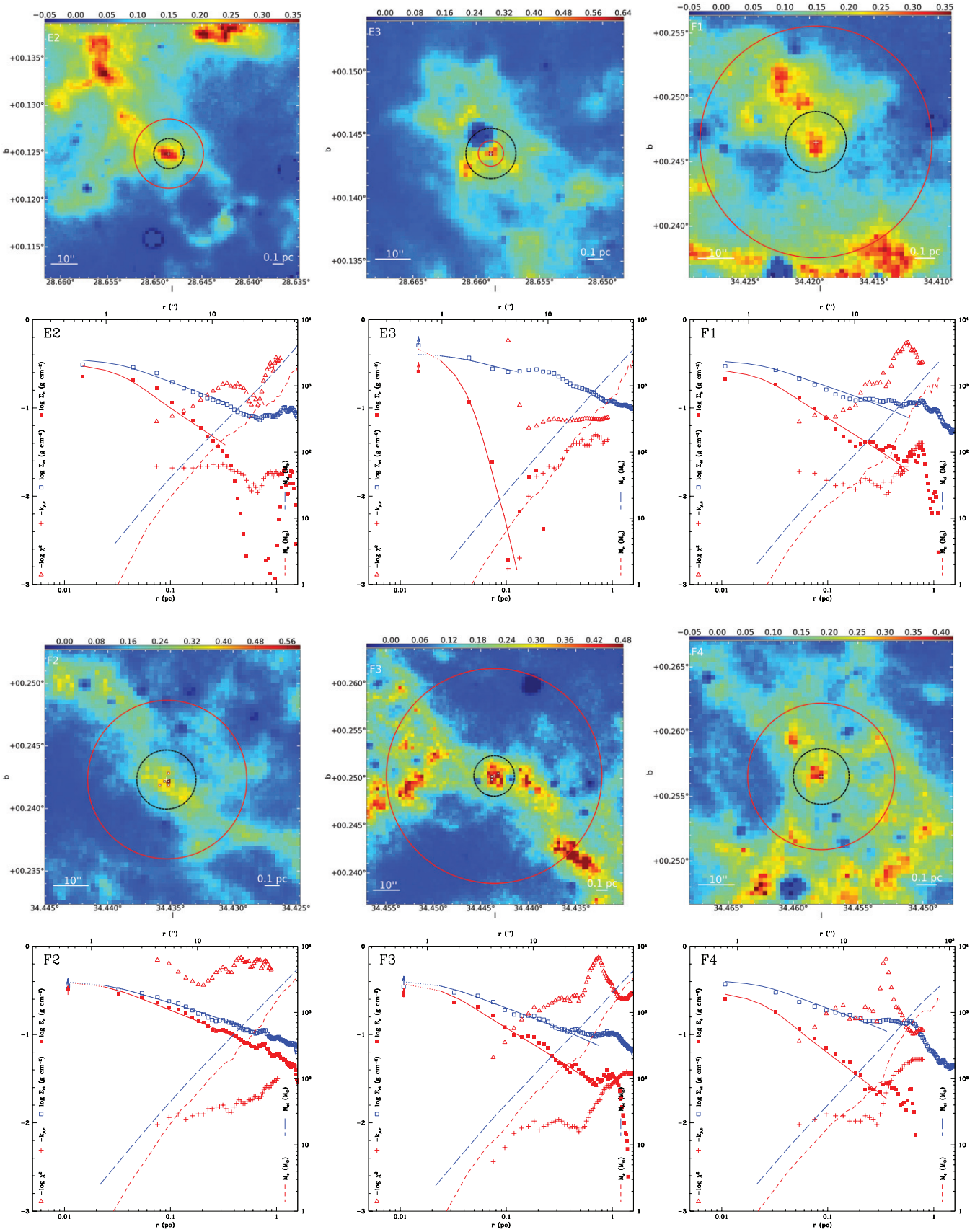

Figure 10. Core E2, E3, F1, F2, F3, and F4 Σ maps (notation as in Figure 5(a)) and azimuthally averaged radial profile figures (notation as in Figure 5(b)). (A color version of this figure is available in the online journal.)

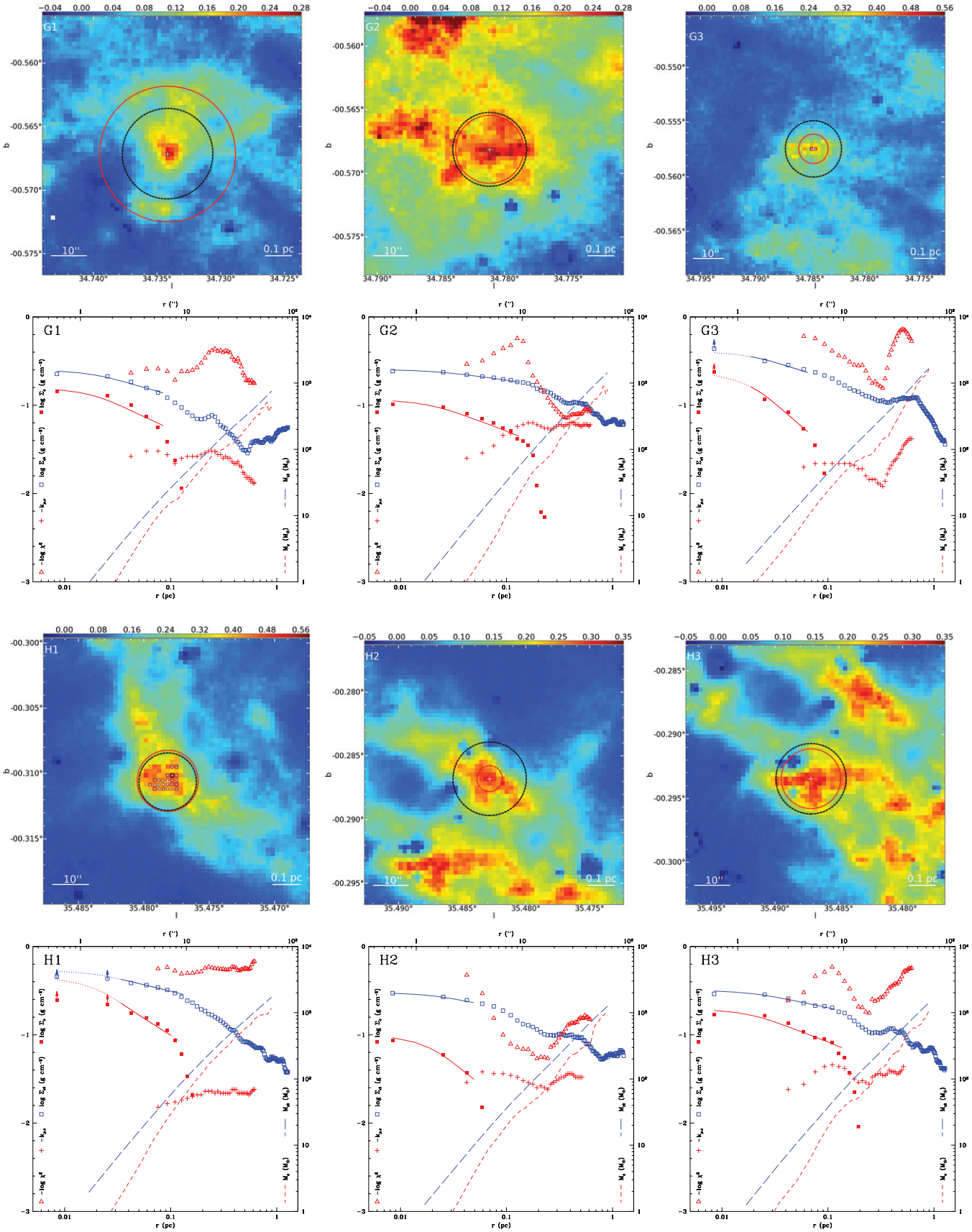

Figure 11. Core G1, G2, G3, H1, H2, and H3 Σ maps (notation as in Figure 5(a)) and azimuthally averaged radial profile figures (notation as in Figure 5(b)). (A color version of this figure is available in the online journal.)

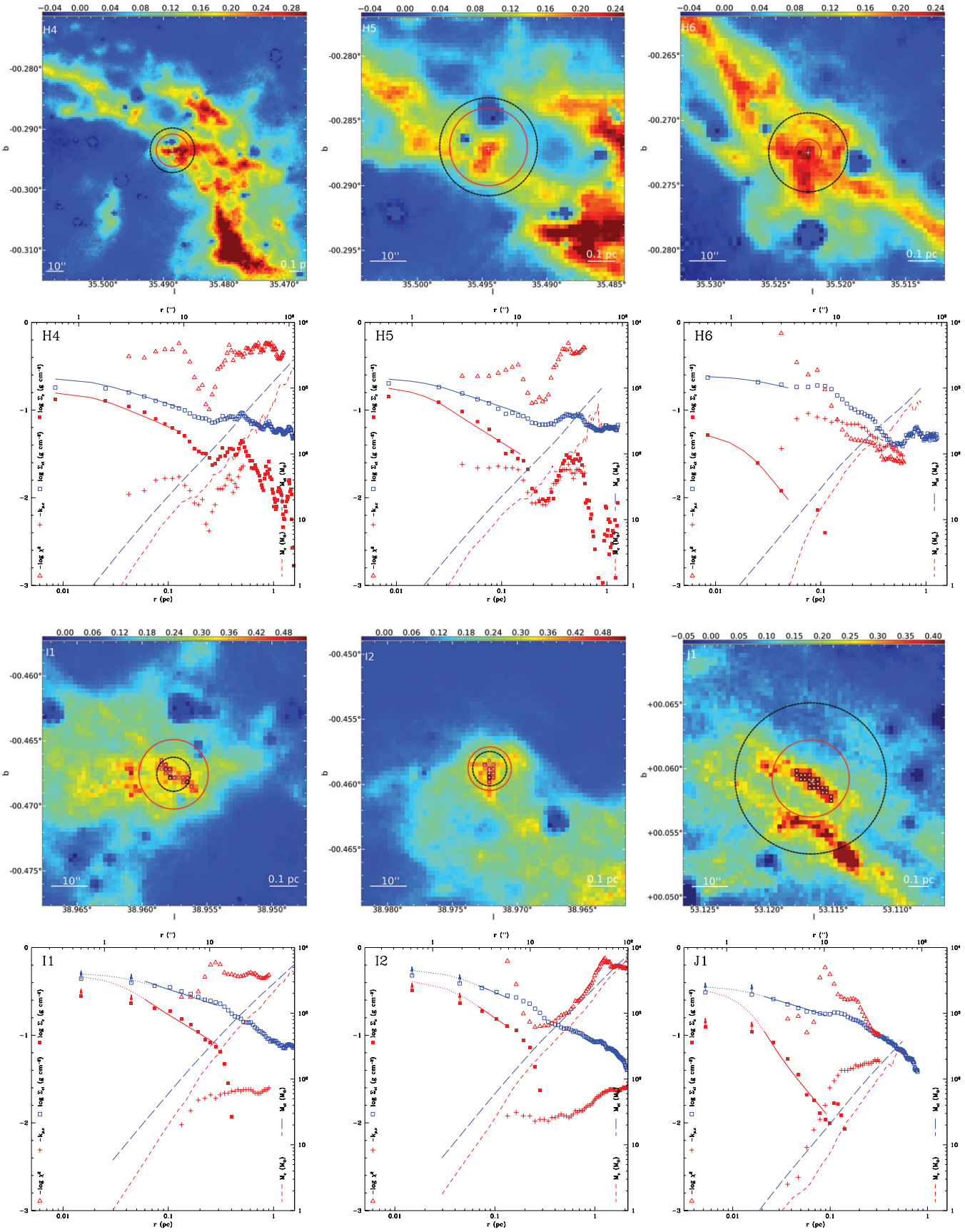

Figure 12. Core H4, H5, H6, I1, I2, and J1 Σ maps (notation as in Figure 5(a)) and azimuthally averaged radial profile figures (notation as in Figure 5(b)). (A color version of this figure is available in the online journal.)

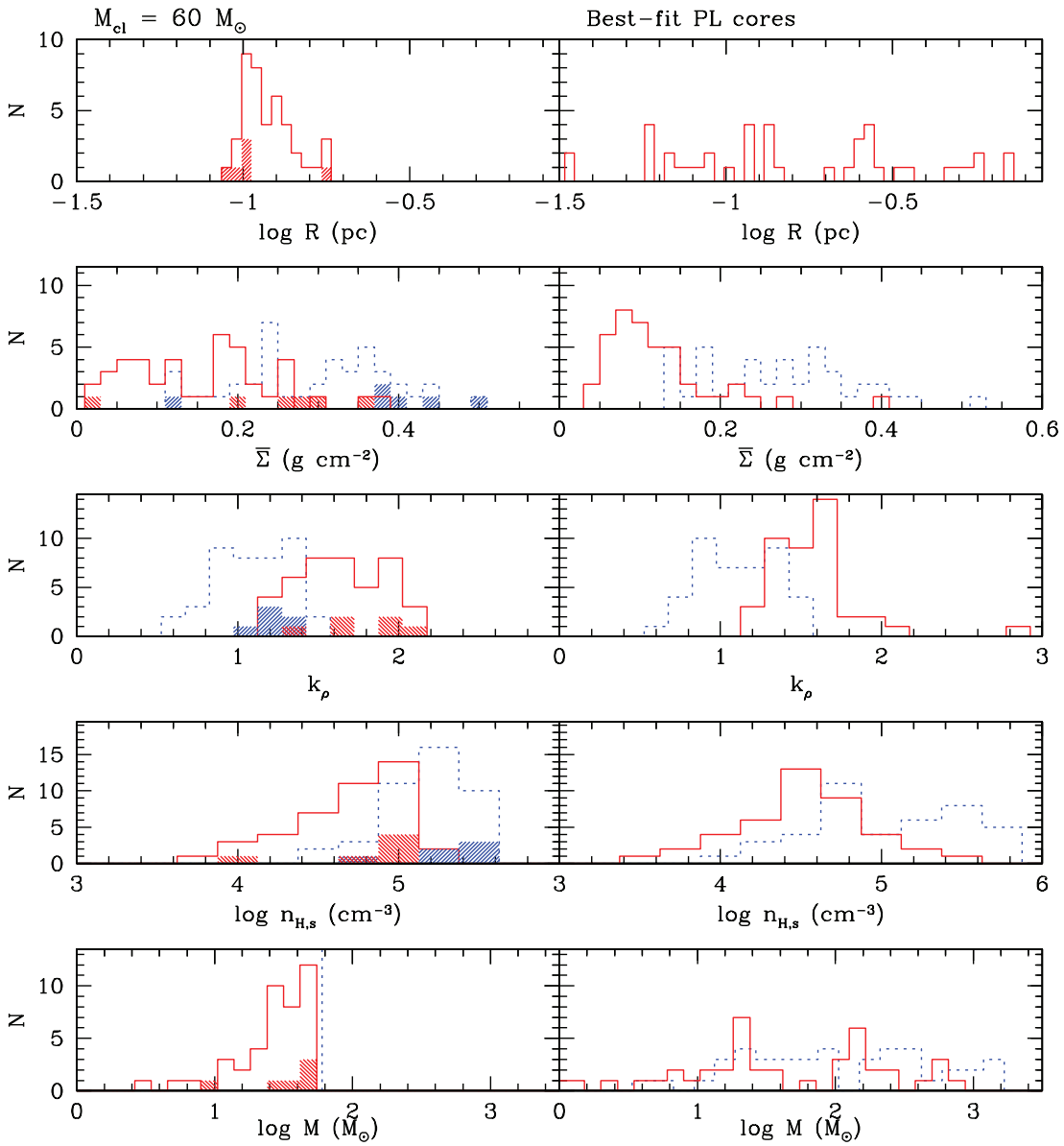

Figure 13. (a) Left column: distributions of properties of clumps and cores at the scale where the observed total enclosed mass $M_{\rm cl} = 60\,M_\odot$, which defines $R_{\rm cl} = R_c$. The first graph shows the distribution of $R_{\rm cl}$ (red solid line) of the 42 cores enclosing this mass. The shaded subset shows the five cores (A1, C2, H1, I1, and I2) that have extended saturation in their centers on this scale. The second panel down shows the mean mass surface density of the clumps, $\bar{\Sigma}_{\rm cl}$ (blue dotted line; shaded subset as before), and cores after clump envelope subtraction, $\bar{\Sigma}_{c,\rm PL}$ (red solid line), based on the power-law fit. The third panel down shows the distributions of $k_{\rho,\rm cl}$ (blue dotted line) and $k_{\rho,c}$ (red solid line). The fourth panel shows the distributions of $n_{{\rm H},s,\rm cl}$ (blue dotted line) and $n_{{\rm H},s,c}$ (red solid line). The bottom panel shows the distribution of $M_{c,\rm PL}$ (red solid line). The vertical blue dotted line shows the 60 $M_\odot$ scale of the clump. (b) Right column: as for (a) but now for the best-fit power law plus clump envelope models. The only difference is that in the bottom panel, the clump mass, $M_{\rm cl}$, is now shown (blue dotted line).

(A color version of this figure is available in the online journal.)

these high Σ objects are surrounded by regions that also have significant mass surface densities. Thus, next we model the cores with a similar PL density structure,

$$\rho_c(r) = \rho_{s,c}\left(\frac{r}{R_c}\right)^{-k_{\rho,c}}, \qquad (7)$$

but now, when comparing to the observed Σ maps, we account for the mass surface density of the surrounding clump medium, $\Sigma_{\rm cl,env}$. We estimate $\Sigma_{\rm cl,env}$ using the observed value in the annular region from R_c to $2R_c$. This choice is motivated by the desire to sample a region of the clump that has a scale comparable to the core in both size and mass.[4] We assume that this same value of $\Sigma_{\rm cl,env}$ covers the area of the core, and so subtract it from the interior $\Sigma_{\rm cl}(r)$ profile to derive the mass surface density profile of the core, $\Sigma_c(r)$. Thus, note that $\Sigma_{\rm cl,env} = \bar{\Sigma}_{\rm cl} - \bar{\Sigma}_c$.

For the same $M_{\rm cl} = 60\,M_\odot$ enclosed mass scale as defined above, we set $R_c = R_{\rm cl}(M_{\rm cl} = 60\,M_\odot)$. The masses contained in the cores, based on integrating the $\Sigma_c(r)$ profile, are of

[4] We have also tried measuring $\Sigma_{\rm cl,env}$ from a thin, 1.″2 wide annulus just outside R_c, which generally leads to larger estimated values of $\Sigma_{\rm cl,env}$. However, we consider that this thin-shell annulus does not sample a large enough region and mass of the clump that, via self-gravity, would be responsible for setting core's surrounding pressure (see discussion in Section 1).

course less than the 60 $M_\odot$ we previously identified with the clump. For Core A1, we derive a core mass of $M_c = 37.9\ M_\odot$ with $\bar{\Sigma}_c = 0.316$ g cm^{-2}. Its value of $k_{\rho,c} = 2.04$ and $n_{\mathrm{H},s,c} = 1.21 \times 10^5$ cm^{-3}, i.e., a steeper density profile with a lower value of the volume density at the surface than was derived previously. For the 42 cores, we find the mean/median/dispersion values of $M_c = 30.4/30.4/12.7\ M_\odot$, $\bar{\Sigma}_c = 0.139/0.160/0.0738$ g cm^{-2}, $k_{\rho,c} = 1.64/1.67/0.271$, and $n_{\mathrm{H},s,c} = (0.639/0.750/0.394) \times 10^5$ cm^{-3} (see red solid line histograms in Figure 13(a) and Tables 2 and 3). Compared to the clump results (i.e., derived from the total Σ profiles), above, for the envelope-subtracted core properties we necessarily find smaller surface densities, steeper density profiles, and smaller volume densities.

The PL fits ignore annuli affected by significant saturation, where Σ is underestimated. Thus, we also estimate a core mass, $M_{c,\mathrm{PL}}$, based on extrapolation of the PL fits to the center of the core:

$$M_{c,\mathrm{PL}} = \frac{4\pi}{3-k_{\rho,c}}\rho_s R_c^3 = \frac{43.5}{3-k_{\rho,c}}\frac{n_{\mathrm{H},s,c}}{10^5\ \mathrm{cm}^{-3}} \times \left(\frac{R_c}{0.1\ \mathrm{pc}}\right)^3 M_\odot \ (k_{\rho,c} < 3). \quad (8)$$

There are no cores where the derived $k_\rho > 3$ for which the inner boundary condition would have to be considered. If there were, then in these cases we would expect to truncate the PL at the Jeans scale in the core. For Core A1, $M_{c,\mathrm{PL}} = 49.2\ M_\odot$, about 30% times larger than M_c. Such an increase is expected since this is one of the most extensively saturated cores. For the rest of the 42 cores, the change is typically much smaller. The mean/median/dispersion values of $M_{c,\mathrm{PL}} = 31.1/31.0/13.5\ M_\odot$ and $\bar{\Sigma}_{c,\mathrm{PL}} = 0.154/0.171/0.0899$ (see red solid line histograms in Figure 13(a) and Tables 2 and 3).

3.2.3. Best-fit Power-law Cores

We now repeat the PL core plus clump envelope fitting procedure as a function of radius, starting at the inner region with three unsaturated annuli for the core. An annulus twice as large in radius is used to estimate the value of Σ of the clump envelope, $\Sigma_{\mathrm{cl,env}}$. We assess the relative goodness of fit of this model as a function of r by finding the minimum of the reduced χ^2 parameter, defined by

$$\chi^2 \equiv \sum_{i=1,N} \frac{1}{\nu}\frac{[\Sigma_{c,\mathrm{PL}}(r) - \Sigma_{c,i}(r)]^2}{\sigma_i^2}, \quad (9)$$

where N is the number of annuli, $\nu = N - 2$ is the number of degrees of freedom, and σ is the error for each annulus, which we take to be $\sigma = 0.01$ g cm^{-2} + $0.2\Sigma_c$. Note that because of the 2″ angular resolution of *Spitzer* IRAC, adjacent annuli are not completely independent. However, the relative values of χ^2 should still give a measure of the best-fitting model.

We place some additional constraints on the fitting. First, we do not allow the best-fit core to extend beyond neighboring core centers (from our sample of 42 cores). Second, to prevent independent discrete structures that are not part of our core sample from influencing the fitting, we check for a 3σ rise in the Σ_c profile by comparing the annulus before any rise begins to the following local maximum. If this occurs, then we ignore fits beyond the pre-rise annulus, and search inward for a local maximum in χ_ν^2 and define that to be the best-fit radius (for example, this occurs in Core A3). Third, if more than 25% of an annulus is composed of MIR emission pixels, then we do not extend the fit any further. In these cases, a prior unaffected annulus with a local maximum in χ_ν^2 is chosen as the best-fit radius (this circumstance only arises in Core E3). As a result of the above constraints, it is possible that the global minimum of χ_ν^2 will not be chosen as the "best fit."

The results for $M_c(r)$, $k_{\rho,c}(r)$, and $-\log\ \chi^2(r)$ are shown for Core A1 in Figure 5(b). The location of the peak value of $-\chi^2$ indicates the best-fitting PL core radius, which occurs at 0.251 pc with a value of $\chi^2 = 1.62$. A circle of this best-fit core radius is shown in the Σ map of the core in Figure 5(a). The total enclosed mass at this scale is $M_{\mathrm{cl}} = 303\ M_\odot$, the core mass is $M_c = 194\ M_\odot$, the mean core mass surface density is $\bar{\Sigma}_c = 0.204$ g cm^{-2}, and the clump surrounding the core has $\Sigma_{\mathrm{cl,env}} = \bar{\Sigma}_{\mathrm{cl}} - \bar{\Sigma}_c = 0.115$ g cm^{-2}. The core mass based on integrating the PL profile is $M_{c,\mathrm{PL}} = 204\ M_\odot$, yielding a slightly higher mean mass surface density of $\bar{\Sigma}_{c,\mathrm{PL}} = 0.214$ g cm^{-2}.

The best-fit total $\Sigma_{\mathrm{cl}}(r) = \Sigma_c(r) + \Sigma_{\mathrm{cl,env}}$ model profile is shown by the solid line in Figure 5(b) (the dotted continuation in the inner region indicates where annuli affected by saturation are not used in the fitting). Figure 5(c) shows the clump envelope-subtracted profile of $\Sigma_c(r)$, together with various projected PL fits, including the best-fit value of $k_{\rho,c} = 1.88$. The parameters of the best-fitting PL plus clump envelope model are listed in Table 2.

The distributions of R_c, $\bar{\Sigma}_{\mathrm{cl}}$ (which is the mean total Σ over the area of the core), $\bar{\Sigma}_{c,\mathrm{PL}}$, $k_{\rho,\mathrm{cl}}$, $k_{\rho,c}$, $n_{\mathrm{H},s,\mathrm{cl}}$, $n_{\mathrm{H},s,c}$, M_{cl}, and $M_{c,\mathrm{PL}}$ are shown in Figure 13(b) and summarized in Table 3. The values for each core are listed in Table 2.

It is important to note that these "best-fit" values may not necessarily be the most accurate description of the core structures. They are based on azimuthally averaged quantities. The Σ map of a particular core should be inspected to gauge the validity of this assumption. Also, the values of χ^2 as a function of radius should be checked to gauge the reasonableness and uniqueness of the fit.

The radii and masses of the best-fit cores are generally, but not always, larger than those at the $M_{\mathrm{cl}} = 60\ M_\odot$ scale, and thus the volume densities are generally lower. The mean/median/dispersion values of $k_{\rho,\mathrm{cl}} = 1.10/1.12/0.246$ and $k_{\rho,c} = 1.58/1.56/0.277$ are, however, very similar to those derived at the $M_{\mathrm{cl}} = 60\ M_\odot$ scale, which suggests that the assumption by McKee & Tan (2002) and MT03 of a self-similar hierarchy of structure from the clumps to core scales is a reasonable one. The fiducial value they adopted of $k_\rho = 1.5$ also is close to the average values found in this sample. In Figure 14, we plot $k_{\rho,c}$ versus $M_{c,\mathrm{PL}}$, $\bar{\Sigma}_{c,\mathrm{PL}}$, and $\Sigma_{\mathrm{cl,env}}$ for the best-fit cores There are no apparent correlations of $k_{\rho,c}$ with these properties.

3.2.4. Best-fit Bonnor–Ebert Cores

We perform a similar analysis as the PL plus constant envelope fitting as a function of radius, but now using critical Bonnor–Ebert (BE) profiles (varying the total effective sound speed, c_s and surface pressure, P_0) plus a constant envelope. See Dapp & Basu (2009) for more details about fitting BE profiles to column density data.

The best-fitting model for Core A1 is shown in Figure 5(d). This has $R_c = 0.670$ pc, $M_c = 353\ M_\odot$, $\bar{\Sigma}_c = 0.0523$ g cm^{-2}, $c_s = 0.275$ km s^{-1}, and $P_0/k = 8.9 \times 10^7$ K cm^{-3}. However, the value of $\chi^2 = 8.75$, which is significantly larger, i.e., worse, than the best-fit PL plus clump envelope model fit (for which

Table 2
Core Properties

Core[a]	l	b	$M_{\rm cl}(< r) = 60\,M_\odot$										Best-fit Power Law										
			$R_{\rm cl} = R_c$ (pc)	$\bar{\Sigma}_{\rm cl}$ (g cm^{-2})	$\bar{\Sigma}_c$ (g cm^{-2})	$k_{\rho,{\rm cl}}$	$k_{\rho,c}$	$n_{{\rm H},s,{\rm cl}}$ (10^5 cm^{-3})	$n_{{\rm H},s,c}$ (10^5 cm^{-3})	M_c ($M_\odot$)	$M_{c,{\rm PL}}$ ($M_\odot$)	$\bar{\Sigma}_{c,{\rm PL}}$ (g cm^{-2})	R_c (pc)	$\bar{\Sigma}_{\rm cl}$ (g cm^{-2})	$\bar{\Sigma}_c$ (g cm^{-2})	$k_{\rho,{\rm cl}}$	$k_{\rho,c}$	$n_{{\rm H},s,{\rm cl}}$ (10^5 cm^{-3})	$n_{{\rm H},s,{\rm c}}$ (10^5 cm^{-3})	$M_{\rm cl}$ ($M_\odot$)	M_c ($M_\odot$)	$M_{c,{\rm PL}}$ ($M_\odot$)	$\bar{\Sigma}_{c,{\rm PL}}$ (g cm^{-2})
A1^{sm}	18.78675	−0.28592	0.0962	0.431	0.316	1.40	2.04	2.47	1.21	37.9	49.2	0.353	0.251	0.319	0.204	1.38	1.88	0.713	0.332	303	194	204	0.214
A2^{s}	18.80117	−0.29625	0.106	0.356	0.205	1.30	1.79	1.96	0.838	34.6	35.9	0.214	0.251	0.298	0.149	1.34	1.42	0.682	0.353	283	141	154	0.162
A3^{s}	18.80750	−0.30550	0.109	0.336	0.249	1.46	2.06	1.64	0.767	44.3	46.0	0.258	0.698	0.180	0.0936	1.48	1.72	0.135	0.0594	1320	686	687	0.0937
B1^{sm}	19.28758	0.08083	0.114	0.307	0.216	1.26	1.68	1.61	0.872	42.1	42.6	0.218	0.251	0.240	0.149	1.28	1.50	0.570	0.307	228	142	141	0.148
B2	19.30758	0.06625	0.134	0.222	0.151	1.10	1.43	1.08	0.579	40.7	38.6	0.144	0.265	0.185	0.113	1.12	1.34	0.452	0.237	195	120	116	0.109
C1	28.32450	0.06655	0.102	0.383	0.119	0.900	1.31	2.72	0.677	18.6	18.5	0.118	0.116	0.382	0.114	0.900	1.38	2.40	0.558	77.8	23.3	23.4	0.115
C2^{sm}	28.34383	0.06017	0.0884	0.510	0.164	1.20	1.96	3.59	0.453	19.2	13.1	0.111	0.0872	0.512	0.165	1.26	1.42	3.53	1.71	58.6	18.9	31.3	0.274
C3	28.35217	0.09450	0.155	0.165	0.0686	1.08	1.45	0.711	0.228	24.9	23.9	0.0659	0.145	0.167	0.0707	1.08	1.44	0.773	0.244	53.4	22.5	20.8	0.0654
C4^{sp}	28.35417	0.07067	0.0958	0.434	0.171	1.09	1.80	2.99	1.67	49.5	53.3	0.386	0.116	0.421	0.158	1.22	1.46	2.24	0.789	85.8	32.2	34.8	0.171
C5	28.35617	0.05650	0.104	0.369	0.0372	0.781	1.30	2.72	0.188	6.04	5.43	0.0335	0.0581	0.403	0.0512	0.800	1.70	5.28	0.390	20.5	2.60	2.56	0.0504
C6	28.36267	0.05150	0.109	0.334	0.177	0.994	1.82	2.13	0.718	31.7	34.3	0.192	0.581	0.258	0.103	0.860	1.26	0.330	0.102	1317	524	501	0.0985
C7	28.36433	0.11950	0.129	0.238	0.0556	1.15	1.45	1.18	0.718	49.2	43.3	0.172	0.0581	0.277	0.0727	1.04	1.58	3.23	0.629	14.1	3.70	3.78	0.0744
C8	28.38783	0.03817	0.111	0.322	0.202	1.16	1.58	1.85	0.895	37.5	37.5	0.202	0.290	0.257	0.137	1.16	1.46	0.567	0.245	327	175	169	0.133
C9	28.39950	0.08217	0.111	0.321	0.160	1.02	1.62	1.99	0.705	29.8	30.4	0.163	0.261	0.277	0.118	1.02	1.36	0.732	0.267	286	121	126	0.122
D1	28.52717	−0.25033	0.109	0.337	0.167	0.956	1.39	2.17	0.885	29.7	31.0	0.178	0.133	0.325	0.154	0.960	1.68	1.71	0.514	86.0	40.9	39.9	0.151
D2	28.53750	−0.27650	0.105	0.361	0.172	0.873	1.77	2.53	0.720	28.6	29.5	0.0622	0.332	0.280	0.0949	0.860	1.22	0.623	0.171	464	156	153	0.0930
D3	28.54150	−0.23517	0.110	0.331	0.0608	0.788	1.55	2.29	0.280	11.0	11.2	0.243	0.0663	0.370	0.0863	0.720	2.02	4.38	0.422	24.4	5.71	5.46	0.0825
D4^{p}	28.53950	−0.26950	0.112	0.318	0.231	0.772	1.29	2.18	1.27	43.5	45.7	0.262	0.0663	0.346	0.254	0.720	1.32	4.10	2.10	22.8	16.8	15.9	0.241
D5^{sm}	28.56533	−0.22783	0.0948	0.443	0.259	0.880	1.92	3.43	1.03	35.1	35.4	0.0461	0.531	0.324	0.145	0.880	1.44	0.445	0.148	1370	614	619	0.146
D6	28.55550	−0.23917	0.126	0.250	0.0495	0.586	1.24	1.66	0.222	11.9	11.0	0.188	0.133	0.249	0.0486	0.700	1.62	1.48	0.168	66.0	12.8	12.5	0.0475
D7^{s}	28.56667	−0.23300	0.0993	0.404	0.168	0.559	1.28	3.43	1.12	24.9	27.9	0.171	0.265	0.364	0.133	0.640	1.54	1.12	0.247	385	141	137	0.130
D8^{s}	28.57283	−0.23267	0.104	0.369	0.169	0.900	1.68	2.57	0.747	27.6	27.7	0.0862	0.497	0.271	0.0756	0.840	1.30	0.408	0.0856	1010	281	269	0.0724
D9	28.58667	−0.22767	0.126	0.250	0.0832	0.834	1.50	1.49	0.355	19.9	20.6	0.0701	0.232	0.231	0.0664	0.840	1.40	0.743	0.165	187	53.8	56.1	0.0693
E1	28.64350	0.13817	0.115	0.301	0.0736	0.947	1.26	1.86	0.383	14.6	14.6	0.0735	0.0890	0.313	0.0826	0.940	1.36	2.50	0.561	37.3	9.85	10.5	0.0886
E2	28.64850	0.12483	0.127	0.246	0.164	1.33	1.66	1.12	0.678	42.2	45.1	0.185	0.267	0.190	0.109	1.38	1.72	0.399	0.177	204	117	115	0.107
E3^{sm}	28.65883	0.14350	0.106	0.352	0.0983	0.980	1.78	2.33	1.35	16.7	29.9	0.176	0.0890	0.335	0.0818	1.48	2.82	4.41	0.175	89.1	21.8	29.9	0.113
F1	34.41950	0.24583	0.141	0.199	0.114	1.36	1.91	0.806	0.317	34.4	35.5	0.118	0.559	0.139	0.0549	1.34	1.60	0.143	0.0466	658	258	253	0.0537
F2^{sp}	34.43517	0.24217	0.118	0.284	0.251	1.36	1.90	1.37	0.828	53.0	53.8	0.255	0.473	0.184	0.151	1.32	1.76	0.227	0.126	622	512	468	0.139
F3^{sm}	34.44383	0.24967	0.127	0.248	0.178	1.50	2.01	1.01	0.513	43.2	46.2	0.191	0.731	0.140	0.0718	1.46	1.76	0.102	0.0419	1133	578	575	0.0714
F4	34.45800	0.25650	0.128	0.241	0.122	1.31	1.98	1.11	0.322	30.4	28.8	0.116	0.344	0.184	0.0664	1.36	1.66	0.304	0.0832	329	118	110	0.0620
G1	34.73417	−0.56683	0.171	0.135	0.0723	1.38	1.54	0.446	0.303	46.3	45.2	0.102	0.0759	0.184	0.101	1.20	1.52	1.50	0.694	15.9	8.72	8.93	0.103
G2	34.78117	−0.56817	0.138	0.209	0.0674	0.860	1.20	1.12	0.289	19.3	18.4	0.0642	0.118	0.213	0.0717	0.860	1.24	1.34	0.366	44.8	15.0	14.9	0.0710
G3^{sm}	34.78483	−0.55750	0.122	0.270	0.0910	1.25	1.67	1.32	0.756	47.1	44.9	0.203	0.0591	0.324	0.123	1.10	1.70	3.59	0.878	17.0	6.46	6.07	0.115
H1^{sm}	35.47800	−0.31033	0.103	0.377	0.166	1.26	1.68	2.19	0.849	26.4	30.6	0.193	0.0843	0.392	0.180	1.20	1.62	2.90	1.21	42.0	19.3	23.0	0.215
H2	35.48283	−0.28700	0.137	0.212	0.0496	1.19	1.55	0.970	0.0872	14.0	6.73	0.0238	0.0337	0.290	0.0680	1.02	1.54	5.91	1.01	4.97	1.16	1.16	0.0679
H3	35.48733	−0.29367	0.131	0.232	0.111	1.08	1.45	1.17	0.437	28.6	27.6	0.107	0.101	0.245	0.123	1.06	1.34	1.63	0.725	37.8	19.0	19.6	0.127
H4	35.48867	−0.28383	0.177	0.126	0.0785	1.34	2.02	0.412	0.148	37.2	36.6	0.0773	0.118	0.142	0.0943	1.36	1.56	0.686	0.398	29.9	19.7	19.8	0.0945
H5	35.49450	−0.28733	0.183	0.119	0.0605	1.32	2.04	0.378	0.0986	30.3	27.4	0.0546	0.134	0.132	0.0730	1.30	1.62	0.587	0.258	36.2	20.0	19.6	0.0718
H6	35.52250	−0.27250	0.145	0.188	0.0166	0.906	1.14	0.947	0.0478	5.28	3.41	0.0107	0.0337	0.228	0.0337	0.900	1.58	4.93	0.471	3.91	0.578	0.553	0.0323
I1^{sm}	38.95783	−0.46783	0.101	0.393	0.227	1.21	1.72	2.39	1.27	34.7	44.6	0.292	0.207	0.343	0.178	1.24	1.72	1.01	0.447	223	116	135	0.208
I2^{s}	38.97217	−0.45950	0.102	0.384	0.227	1.32	1.92	2.18	0.933	35.4	39.9	0.256	0.0593	0.439	0.272	1.54	1.60	3.73	3.31	23.2	14.4	21.5	0.407
J1^{spm}	53.11683	0.05917	0.179	0.123	0.0282	0.992	1.34	0.482	0.105	13.7	15.9	0.0327	0.0733	0.147	0.0447	1.18	2.08	1.26	0.369	11.9	3.61	6.88	0.0852

Notes. [a] Core designation from BT09. "^{s}" indicates core is saturated; "^{p}" indicates core's central position has been moved out of the original core boundary from Rathborne et al. (2006); "^{m}" indicates the intensity minimum within the IRDC boundary occurs in this core.

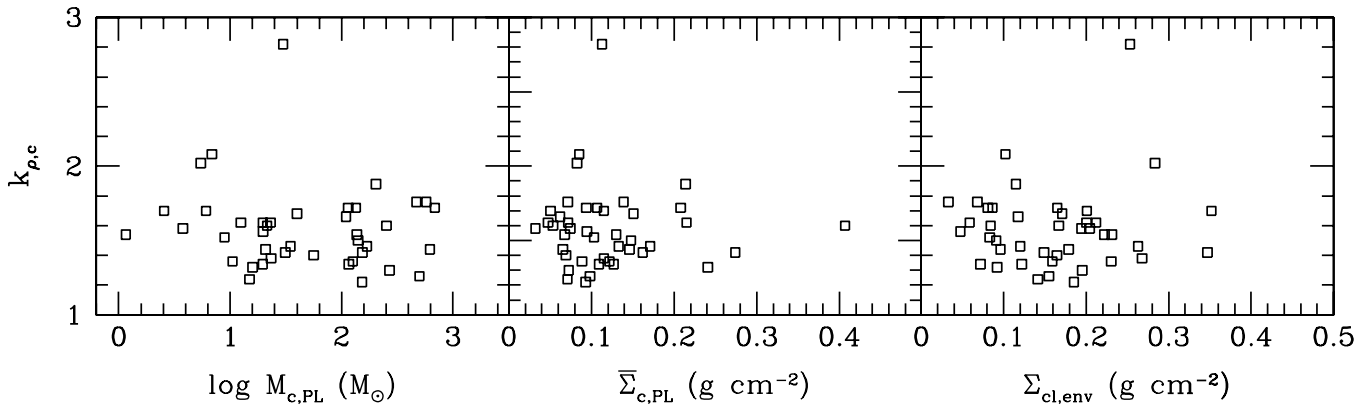

Figure 14. $k_{\rho,c}$ vs. $M_{c,\rm PL}$, $\bar{\Sigma}_{c,\rm PL}$, and $\Sigma_{\rm cl,env}$ for the best-fit cores.

Table 3
Properties of IRDC Core and Clump Sample

Mass Scale	Property	Mean	Median	Dispersion
$M_{\rm cl}(<r)=60\,M_\odot$[a]	$R_{\rm cl}=R_c$ (pc)	0.121	0.114	0.0238
...	$\bar{\Sigma}_{\rm cl}$ (g cm^{-2})	0.296	0.318	0.0952
...	$k_{\rho,\rm cl}$	1.09	1.10	0.236
...	$n_{\rm H,\it s,cl}$ (10^5 cm^{-3})	1.76	1.85	0.852
...	M_c ($M_\odot$)	30.4	30.4	12.7
...	$\bar{\Sigma}_c$ (g cm^{-2})	0.139	0.160	0.0738
...	$k_{\rho,\rm c}$	1.64	1.67	0.271
...	$n_{\rm H,\it s,c}$ (10^5 cm^{-3})	0.639	0.750	0.394
...	$M_{c,\rm PL}$ ($M_\odot$)	31.1	31.0	13.5
...	$\bar{\Sigma}_{c,\rm PL}$ (g cm^{-2})	0.154	0.171	0.0899
Best-fit PL + env.[b]	$M_{\rm cl}$ ($M_\odot$)	279	86.0	392
...	R_c (pc)	0.222	0.134	0.187
...	$\bar{\Sigma}_{\rm cl}$ (g cm^{-2})	0.274	0.277	0.0925
...	$k_{\rho,\rm cl}$	1.10	1.12	0.246
...	$n_{\rm H,\it s,cl}$ (10^5 cm^{-3})	1.76	1.12	1.63
...	M_c ($M_\odot$)	128	32.2	185
...	$\bar{\Sigma}_c$ (g cm^{-2})	0.113	0.103	0.0535
...	$k_{\rho,\rm c}$	1.58	1.56	0.277
...	$n_{\rm H,\it s,c}$ (10^5 cm^{-3})	0.515	0.354	0.616
...	$M_{c,\rm PL}$ ($M_\odot$)	128	34.8	181
...	$\bar{\Sigma}_{c,\rm PL}$ (g cm^{-2})	0.121	0.107	0.0708

Notes.
[a] Mass scale set by the enclosed mass in the Σ map being equal to 60 $M_\odot$.
[b] Mass scale set by the best-fit power-law plus clump envelope model.

$\chi^2 = 1.62$). Also, the size of the BE fitted core is much larger than the PL model: as can be seen from Figure 5(a), on these larger scales the assumption of single monolithic and azimuthally symmetric structure becomes less valid.

Carrying out the BE analysis for all 42 cores, we find that the fits are generally worse than for the PL models. The best-fitting BE radii are typically larger than those of the PL core models. For these reasons, we do not consider the BE models further in our discussion.

4. DISCUSSION AND CONCLUSIONS

We have presented a new method to accurately probe mass surface densities in the range ∼0.01 to ∼0.5 g cm^{-2} on arcsecond scales in quiescent IRDCs, some of which are likely to be the sites of future star formation. The method uses the SMF method of background interpolation from regions around a defined IRDC (BT09) and then estimates the level of foreground emission by seeing if there are *independent, nearby, saturated cores* within the IRDC. If so, then the foreground level is set equal to that observed toward these saturated regions. The resulting Σ measurements derived from this MIREX mapping depend on the assumed MIR dust opacity per unit total mass, but do not depend on the dust temperature, which is a distinct advantage over measurements based on submillimeter/millimeter dust continuum emission.

Focusing on 42 core/clumps within 10 IRDCs, we have tried various methods of characterizing their azimuthally averaged structure. Our preferred method, following the model of McKee & Tan (2002, 2003), involves fitting PL cores surrounded by a clump envelope, which is assumed to have a constant value of Σ that can be estimated from the surrounding region. We have fitted these models as a function of radius from the core center, deriving an overall best fit, but also presenting the full results of this radial characterization. The typical value of the volume density PL index that best describes the cores is $k_{\rho,c} \simeq 1.6$. This is close to the fiducial value of 1.5 adopted by McKee & Tan (2002, 2003), who based their choice on previous measurements on the larger, ∼parsec, scales of gas clumps. We find this PL index does not appear to vary significantly with scale (i.e., between the 60 $M_\odot$ enclosed mass scale and the best-fit PL plus clump scale), nor with other core or clump properties, suggesting the presence of a self-similar hierarchy of structure.

On the scale at which the total projected enclosed mass is 60 $M_\odot$, the derived cores have about 50% of this mass. If massive star formation is to occur, then this is the material that has a high probability of being incorporated into the massive star. These cores have typical radii of ≃0.1 pc, masses of ∼30 $M_\odot$, mean mass surface densities of $\bar{\Sigma}_c \simeq 0.15$ g cm^{-2} and surrounding clump mass surface densities of similar values. If one regards our method of clump envelope subtraction to be an overestimate, then one can consider the typical properties of the clumps on these scales as being representative of the gas that will form massive stars, i.e., with $M_{\rm cl} = 60\,M_\odot$ and $\Sigma_{\rm cl} \simeq 0.3$ g cm^{-2}.

The above values of $\Sigma_{\rm cl}$ are lower by factors of ∼3–7 than the fiducial value of 1 g cm^{-2} considered by McKee & Tan (2002, 2003). Note that their theoretical model is general and does not require a particular value of $\Sigma_{\rm cl}$, so this difference does not require any physical explanation. However, Krumholz & McKee (2008) have proposed that massive star formation requires $\Sigma_{\rm cl} \gtrsim 1$ g cm^{-2}, based on a model in which fragmentation of massive cores is prevented by radiative heating from surrounding lower-mass protostars. The high value of $\Sigma_{\rm cl}$ is required so that the lower-mass protostars accrete at high enough rates that they are luminous enough to sufficiently heat the massive core.

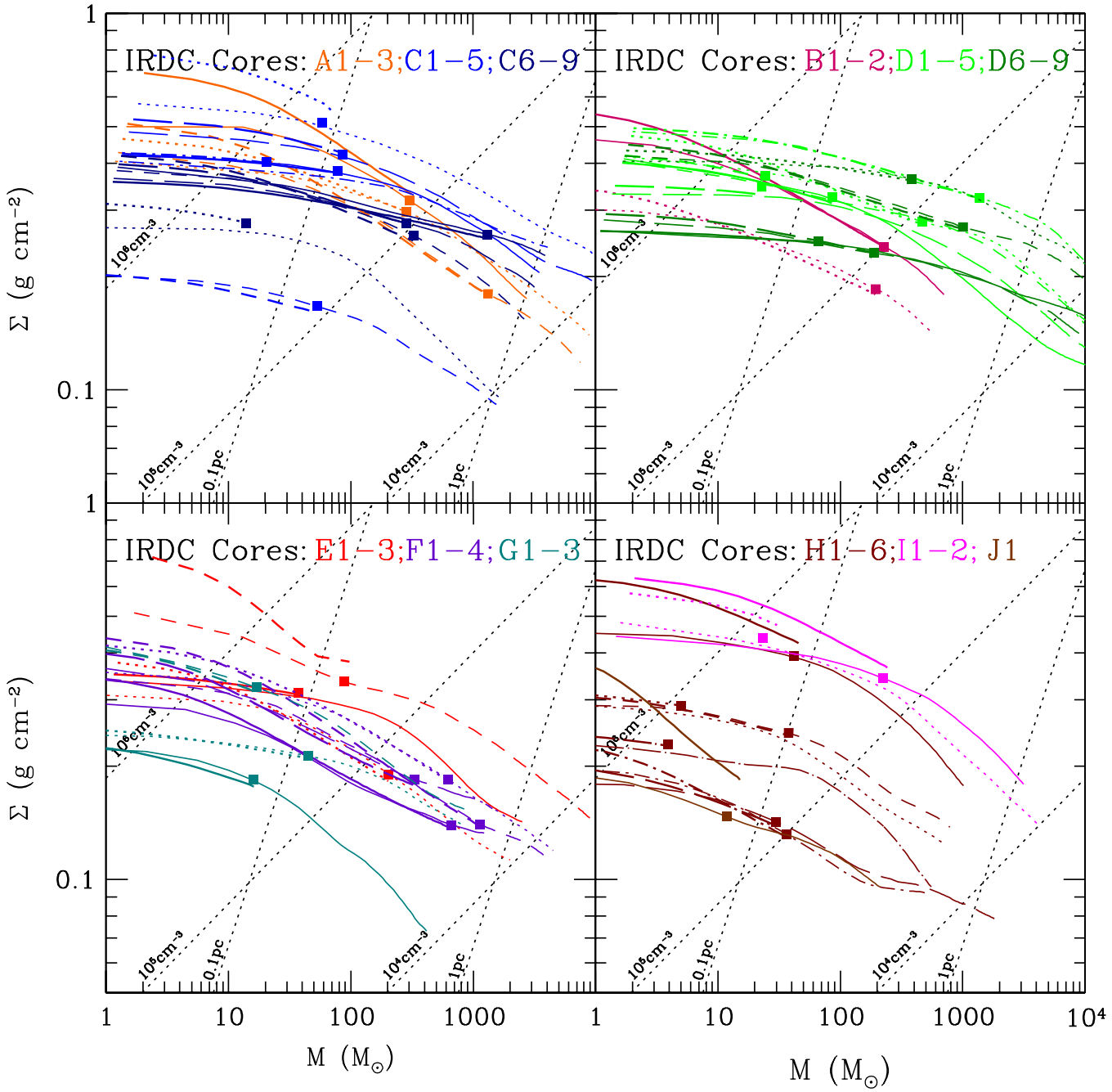

Figure 15. Mass surface density vs. mass ($\Sigma - M$) diagram (including lines of constant radial size and density [$n_{\rm H}$] for spherical clouds) for the 42 IRDC core/clumps. For each range of core numbers, the total mass surface density, $\Sigma_{\rm cl}$, of the cores are indicated by color-coded thin solid, dotted, dashed, long-dashed, dot-dashed, dot-long-dashed lines in order of increasing number (e.g., C1 (solid) to C5 (dot dashed); C6 (solid) to C9 (long dashed)). Squares mark the location of the best-fit cores. Heavier lines extend inward from near the squares show $\Sigma_{c,\rm PL} + \bar{\Sigma}_{\rm cl,env}$, i.e., based on the fitted power-law density profile.

(A color version of this figure is available in the online journal.)

Since massive star formation occurs relatively rarely, it may be that it occurs preferentially in cores with higher values of Σ_c and $\Sigma_{\rm cl}$ than we have observed for the average of our sample, which we note does show significant dispersion. However, we consider this unlikely given that we have selected the highest Σ regions from 10 IRDCs that show some of the highest contrast against the Galactic MIR background (selected from the larger sample of 38 IRDCs studied by Rathborne et al. 2006).

Saturation limits our Σ maps to values of $\simeq$0.5 g cm^{-2} and this may be affecting our ability to find the highest Σ cores. However, we are excluding the saturated regions when deriving core and clump density profiles and most cores do not exhibit extensively saturated centers. We expect our choice of MIR opacity per unit gas mass may be uncertain by $\sim$30% (see Section 1), so this by itself is unlikely to explain the relatively low values of Σ that we are deriving compared to the Krumholz & McKee (2008) prediction.

Another possibility is that these cores and clumps will evolve to higher values of Σ before massive star formation occurs. Indeed, the fact that these are IR dark objects suggests that they cannot yet be experiencing much radiative heating. However, there is observational evidence for star formation activity in

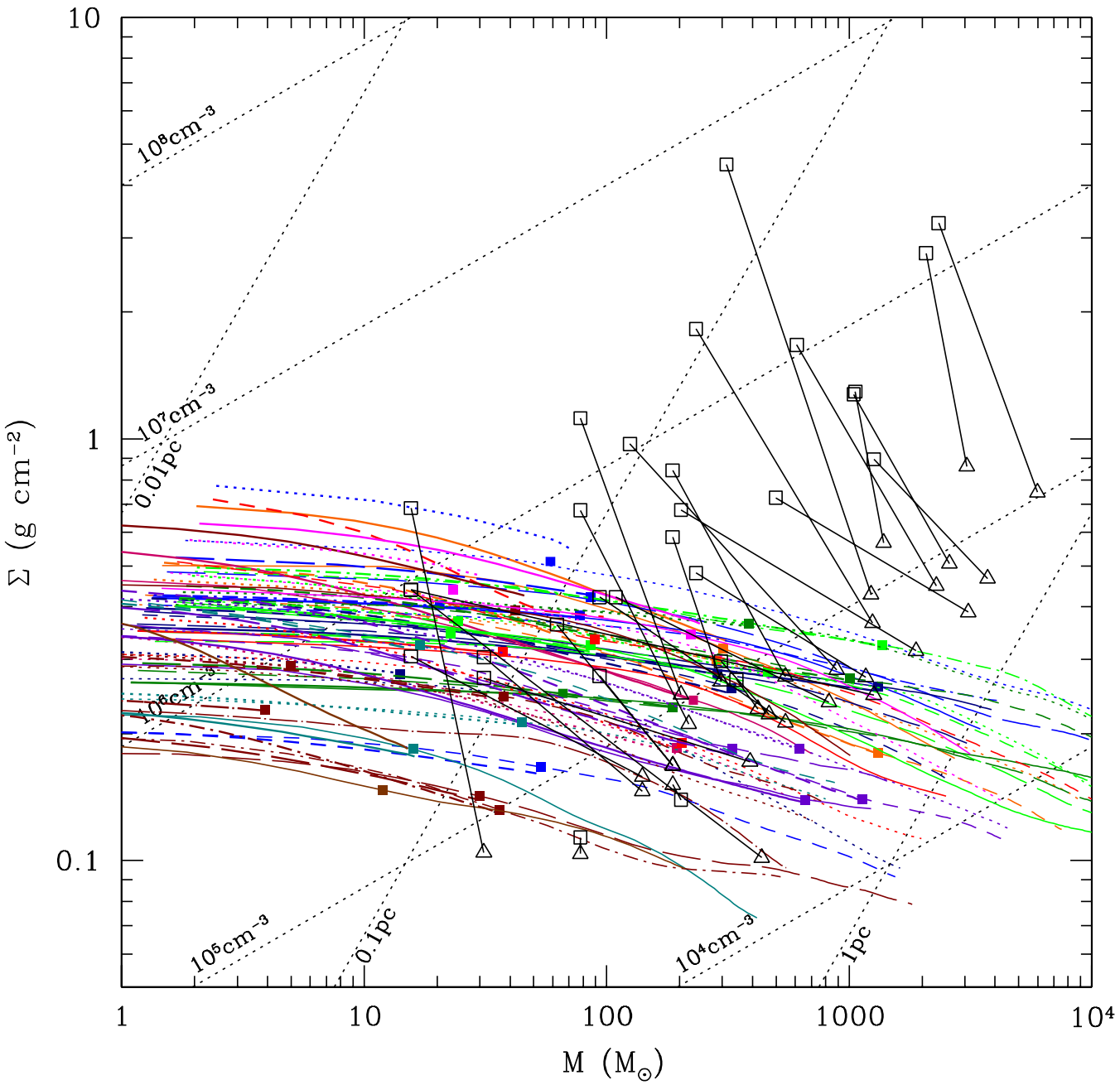

Figure 16. Same as Figure 15, now combining all 42 cores together (colored lines). The black symbols and lines show the masses of 31 actively star-forming core/clumps from Mueller et al. (2002), with triangles indicating the masses above a density threshold of $n_{\rm H} \sim 3 \times 10^4$ cm^{-3} (we have scaled the masses by a factor 1.56 to be consistent with our adopted gas-to-dust mass ratio) and the squares indicating the masses inside the deconvolved source size. Note that the properties of the clouds on this inner scale are not directly resolved, but are inferred based on simple one-dimensional radiative transfer modeling. The IRDC cores/clumps overlap only with the lower-Σ range of the star-forming core/clump sample, perhaps indicating that there is an evolutionary growth in core/clump density as star formation proceeds.

(A color version of this figure is available in the online journal.)

some of these cores. For example, Wang et al. (2006) observed water maser emission located 4.″31 from the center of Core C1. Wang et al. (2011) have reported protostellar outflows from Core C2.

To better compare our IRDC core/clump sample with more evolved systems, in Figure 15 we show the 42 core/clumps on the Σ versus M diagram (following Tan 2007). Here, Σ is measured from the total observed mass inside a given radial distance from the core/clump center. In Figure 16, we compare these profiles to the properties of the 31 star-forming clumps whose IR and submillimeter dust continuum emission was observed and modeled by Mueller et al. (2002). Note that these properties depend on the (one-dimensional) modeled temperature structure, dust emissivity (they used the same Ossenkopf & Henning (1994) dust model that we have adopted for our MIREX maps) and gas-to-dust ratio (we have scaled Mueller et al.'s (2002) masses by a factor 1.56 to be consistent with our adopted gas-to-dust ratio).

The IRDC cores/clumps overlap only with the lower-Σ range of the star-forming core/clump sample, perhaps indicating there is a (physically plausible) evolutionary growth in core/clump density as star formation proceeds. However, note that many

(indeed most) star-forming cores and clumps have $\Sigma < 1\,\mathrm{g\,cm^{-2}}$. Alternatively, the lack of starless high Σ core/clumps may be due to the somewhat smaller volume of the Galaxy that we have probed with our nearby IRDC sample, compared to the Mueller et al. star-forming core/clump sample.

Mueller et al. (2002) found density PL indices of $k_{\rho,\mathrm{cl}} = 1.8 \pm 0.4$, slightly steeper than our derived values for IRDC cores of $k_{\rho,c} \simeq 1.6$, but significantly steeper than our value for clumps of $k_{\rho,\mathrm{cl}} \simeq 1.1$. Again, this latter difference may indicate an evolution in cloud properties as star formation proceeds.

Considering the above results, we suggest that the initial conditions of local massive star formation in the Galaxy may be better characterized with values of $\Sigma_{\mathrm{cl}} \simeq 0.2\,\mathrm{g\,cm^{-2}}$ rather than $1\,\mathrm{g\,cm^{-2}}$, which would imply smaller accretion rates and longer formation times that the fiducial values of MT03. The accretion rate becomes

$$\dot{m}_* = 1.37 \times 10^{-4} \left(\frac{m_{*f}}{30\,M_\odot}\right)^{3/4} \left(\frac{\Sigma_{\mathrm{cl}}}{0.2\ \mathrm{g\ cm^{-2}}}\right)^{3/4} \times \left(\frac{m_*}{m_{*f}}\right)^{0.5} M_\odot\ \mathrm{yr}^{-1} \quad (10)$$

for a core with $k_{\rho,c} = 1.5$ and a star formation efficiency of 50%, where m_* is the instantaneous protostellar mass and m_{*f} is the final protostellar mass. The star formation timescale becomes

$$t_{*f} = 4.31 \times 10^5 \left(\frac{m_{*f}}{30\,M_\odot}\right)^{1/4} \left(\frac{\Sigma}{0.2\ \mathrm{g\ cm^{-2}}}\right)^{-3/4} \mathrm{yr}. \quad (11)$$

In this case of massive star formation at relatively low values of Σ, we expect fragmentation of the cores is prevented by magnetic fields, i.e., if the core mass is equal to the magnetic critical mass (Bertoldi & McKee 1992)

$$M_B = 1020 \left(\frac{R}{Z}\right)^2 \left(\frac{\bar{B}}{30\,\mu\mathrm{G}}\right)^3 \left(\frac{\bar{n}_{\mathrm{H}}}{10^3\ \mathrm{cm^{-3}}}\right)^{-2} M_\odot, \quad (12)$$

where R and Z are the major and minor axes of the core, $\bar{B}$ is the mean field strength in the core, and $\bar{n}_{\mathrm{H}}$ is the mean number density of H nuclei. Thus, for a core with $\bar{n}_{\mathrm{H}} = 10^5\ \mathrm{cm^{-3}}$ and $M_c = 100\,M_\odot$, typical of our sample, the condition $M_B = M_c$ requires a field strength

$$\bar{B} = 300 \left(\frac{M_B}{100\,M_\odot}\right)^{1/3} \left(\frac{Z}{R}\right)^{2/3} \left(\frac{\bar{n}_{\mathrm{H}}}{10^5\ \mathrm{cm^{-3}}}\right)^{2/3} \mu\mathrm{G}. \quad (13)$$

If cores have some significant magnetic support, then we expect $R/Z > 1$, perhaps $\sim$2, so that the required field strength in Equation (12) is then $190\,\mu$G. Such field strengths are similar to those observed in regions of active massive star formation (e.g., Crutcher 2005). Indeed, Crutcher (2005) noted the observed mass to flux ratios scattered about the critical value. Numerical simulations of the collapse of marginally magnetically critical (rather than super critical; e.g., Wang et al. 2010; Hennebelle et al. 2011) cores are required to investigate this scenario for forming massive stars, and, more generally, for explaining the high-mass tail of the initial mass function (Kunz & Mouschovias 2009).

M.J.B. acknowledges support from a Sigma Xi Grant in Aid of Research. J.C.T. acknowledges support from NSF CAREER grant AST-0645412; NASA Astrophysics Theory and Fundamental Physics grant ATP09-0094; NASA Astrophysics Data Analysis Program ADAP10-0110, and a Faculty Enhancement Opportunity grant from the University of Florida. We thank Peter Barnes, Paola Caselli, Ed Churchwell, Francesco Fontani, Audra Hernandez, Jouni Kainulainen, Jens Kauffmann, Shuo Kong, Mark Krumholz, Chris McKee, Thushara Pillai, Sven Van Loo, and Qizhou Zhang for helpful discussions.

REFERENCES

Battersby, C., Bally, J., Jackson, J. M., et al. 2010, ApJ, 721, 222
Bertoldi, F., & McKee, C. F. 1992, ApJ, 395, 140
Beuther, H., Schilke, P., Menten, K. M., et al. 2002, ApJ, 566, 945
Bonnell, I. A., Clarke, C. J., Bate, M. R., & Pringle, J. E. 2001, MNRAS, 324, 573
Bontemps, S., Motte, F., Csengeri, T., & Schneider, N. 2010, A&A, 524, A18
Butler, M. J., & Tan, J. C. 2009, ApJ, 696, 484
Crutcher, R. M. 2005, in IAU Symp. 227, Massive Star Birth: A Crossroads of Astrophysics, ed. R. Cesaroni, M. Felli, E. Churchwell, & M. Walmsley (Cambridge: Cambridge Univ. Press), 98
Dapp, W. B., & Basu, S. 2009, MNRAS, 395, 1092
Draine, B. T. 2003, ApJ, 598, 1017
Draine, B. T. 2011, ApJ, 732, 100
Egan, M. P., Shipman, R. F., Price, S. D., et al. 1998, ApJ, 494, L199
Fontani, F., Palau, A., Caselli, P., et al. 2011, A&A, 529, L7
Hennebelle, P., Commercon, B., Joos, M., et al. 2011, A&A, 528, 72
Hernandez, A. K., & Tan, J. C. 2011, ApJ, 730, 44
Hernandez, A. K., Tan, J. C., Caselli, P., et al. 2011, ApJ, 738, 11
Jackson, J. M., Rathborne, J. M., Shah, R. Y., et al. 2006, ApJS, 163, 145
Kainulainen, J., Alves, J., Beuther, H., et al. 2011, A&A, 536, 48
Kainulainen, J., & Tan, J. C. 2012, A&A, submitted
Krumholz, M. R., & McKee, C. F. 2008, Nature, 451, 1082
Kunz, M. W., & Mouschovias, T. Ch. 2009, MNRAS, 399, L94
Kurayama, T., Nakagawa, A., Sawada-Satoh, S., et al. 2011, PASJ, 63, 513
McKee, C. F., & Tan, J. C. 2002, Nature, 416, 59
McKee, C. F., & Tan, J. C. 2003, ApJ, 585, 850 (MT03)
Mueller, K. E., Shirley, Y. L., Evans, N. J., II, & Jacobson, H. R. 2002, ApJS, 143, 469
Ossenkopf, V., & Henning, T. 1994, A&A, 291, 943
Perault, M., Omont, A., Simon, G., et al. 1996, A&A, 315, L165
Peretto, N., & Fuller, G. A. 2009, A&A, 505, 405
Ragan, S. E., Bergin, E. A., & Gutermuth, R. A. 2009, ApJ, 698, 324
Rathborne, J. M., Jackson, J. M., & Simon, R. 2006, ApJ, 641, 389
Reach, W. T., Rho, J., Tappe, A., et al. 2006, AJ, 131, 1479
Shu, F. H., Adams, F. C., & Lizano, S. 1987, ARA&A, 25, 23
Simon, R., Jackson, J. M., Rathborne, J. M., & Chambers, E. T. 2006, ApJ, 639, 227
Tan, J. C. 2007, in IAU Symp. 237, Triggered Star Formation in a Turbulent ISM, ed. B. G. Elmegreen & J. Palous (Cambridge: Cambridge Univ. Press), 258
van der Tak, F. F. S., van Dishoeck, E. F., Evans, N. J., II, & Blake, G. A. 2000, ApJ, 537, 283
Wang, K., Zhang, Q., Wu, Y., & Zhang, H. 2011, ApJ, 735, 64
Wang, P., Li, Z.-Y., Abel, T., & Nakamura, F. 2010, ApJ, 709, 27
Wang, Y., Zhang, Q., Rathborne, J. M., Jackson, J., & Wu, Y. 2006, ApJ, 651, L125

The Astrophysical Journal, 766:66 (2pp), 2013 March 20 doi:10.1088/0004-637X/766/1/66

ERRATUM: "MID-INFRARED EXTINCTION MAPPING OF INFRARED DARK CLOUDS. II. THE STRUCTURE OF MASSIVE STARLESS CORES AND CLUMPS" (2012, ApJ, 754, 5)

Michael J. Butler[1] and Jonathan C. Tan[2]
[1] Department of Astronomy, University of Florida, Gainesville, FL 32611, USA
[2] Departments of Astronomy & Physics, University of Florida, Gainesville, FL 32611, USA
Received 2012 October 22; published 2013 March 7

Online-only material: color figures

In Figures 3 and 4, the coordinates displayed are not correct for all panels except for the panel displaying cloud D. The size of this error was a ∼0.1 degree offset in the displayed coordinates. We have added the images with corrected coordinates for these panels. In Figure 12, the upper panel for core H4 mistakenly displays an image of core H3. The corrected panel displays core H4. The reference to Draine (2011) listed in the References section is incorrect. The correct reference is Draine, B. T. 2011, Physics of the Interstellar and Intergalactic medium (Princeton, NJ: Princeton Univ. Press). Additionally, in Table 1, the effective radii, $R_{\rm eff}$, listed are effective diameters. These errors have no effect on the results given in the text and data tables.

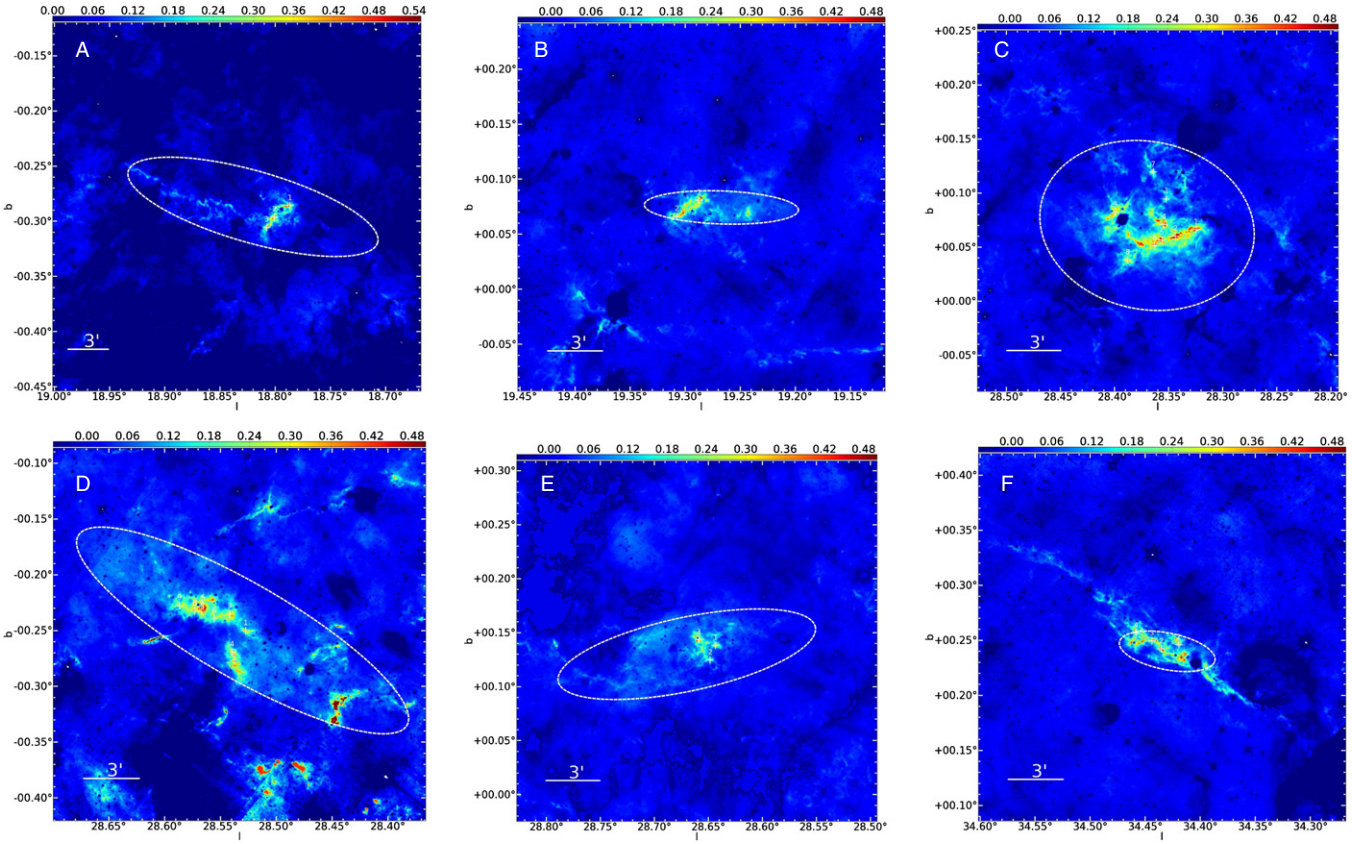

Figure 3. Mass surface density, $\Sigma_{\rm SMF}$, maps of IRDCs A–F derived from MIREX mapping using *Spitzer* IRAC 8 μm images with pixel scale of 1.″2 and angular resolution of 2″ using a saturation-based estimate of the foreground emission (Section 2). The color scale is indicated in g cm^{-2}. The dashed ellipse, defined by Simon et al. (2006) based on MSX images, defines the region where the background emission is estimated not directly from the small-scale median filter average of the image intensity, but rather by interpolation from nearby regions just outside the ellipse. The locations of the massive starless cores we have selected for analysis (Section 3) are marked with crosses. Bright MIR sources appear as artificial "holes" in the map, where we have set the values of $\Sigma = 0$ g cm^{-2}.

(A color version of this figure is available in the online journal.)

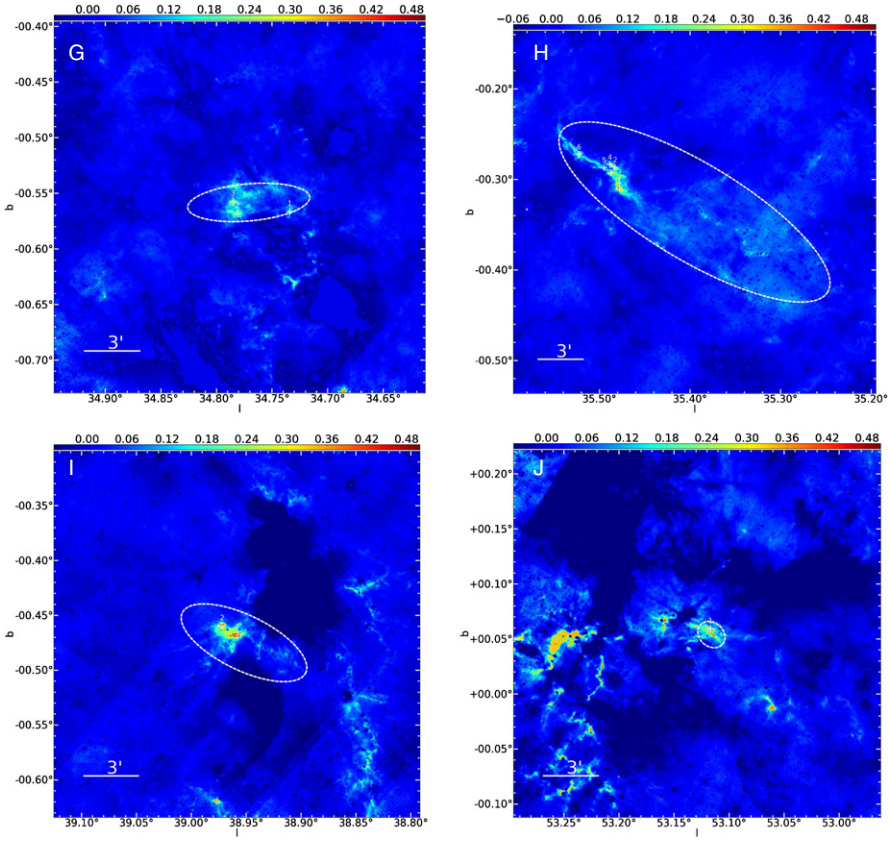

Figure 4. Mass surface density, Σ_{SMF} maps (in the same format as Figure 3) of IRDCs G–J derived from MIREX mapping using *Spitzer* IRAC 8 μm images.
(A color version of this figure is available in the online journal.)

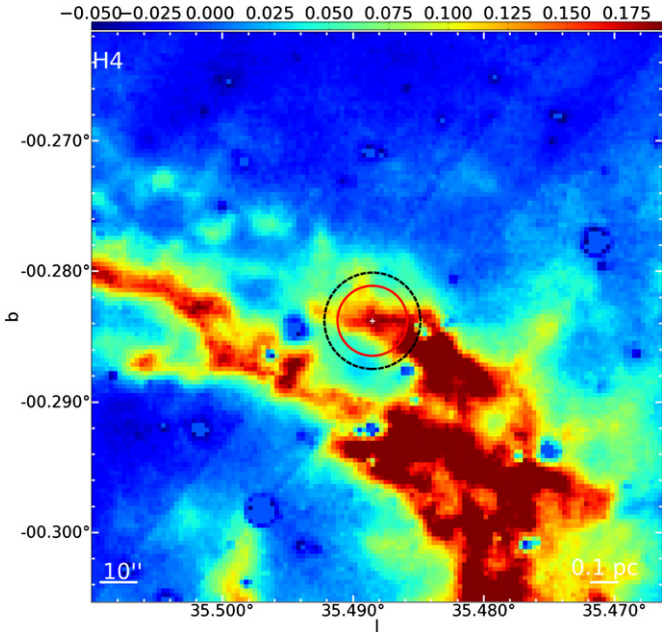

Figure 12. Corrected first panel of Figure 12 showing the mass surface density, Σ_{SMF}, map in g cm^{-2} of IRDC Core H4.
(A color version of this figure is available in the online journal.)

REFERENCES

Draine, B. T. 2011, Physics of the Interstellar and Intergalactic medium (Princeton, NJ: Princeton Univ. Press)
Simon, R., Jackson, J. M., Rathborne, J. M., & Chambers, E. T. 2006, ApJ, 639, 227